PROCEEDING OF OCEAN, MECHANICAL AND AEROSPACE

SCIENCE AND ENGINEERING





PROCEEDING

The 1stInternational Conference on Ocean, Mechanical & Aerospace - Scientists & Engineers -



19th – 20nd November 2014 Resty Menara Hotel, Pekanbaru, Indonesia

Organized by:







Vol.1: 19-November 2014

Contents

About OMAse

Scope of JOMAse

Section IV: Thermodynamic and Structures

Title and Authors	Pages
Effect of Bending Angle Variation to the Strength of Steel Reinforcement Bar Kana Sabatul Ikhwan, M. Dalil	133 - 138
Study on Performance of Double Acting Tanker in Ice Condition <i>Efi Afrizal, Jaswar Koto</i>	139 - 144
Potential Threat to Ship and Port Security-Case Study Meifal Ruslia, Lovely Sona, Mulyadi Bura, Agus Arismana	145 - 149
Performance of Air Conditioning Water Heater with Trombone Coil Type as Dummy Condenser at Different Cooling Loads **Azridjal Aziz, Arya Bhima Satria**	150 - 154
Hydroxyapatite Powder Prepared by Low Temperature Hydrothermal Method from Sea Shells Ahmad Fadli, Fajril Akbar, Pancasila Putri, Dewi Indah Pratiwi, Ikhbal Muhara	155 - 160

ISOMAse

Vol.1: 19-November 2014

Section IV: Thermodynamic and Structures

Title and Authors	Pages
Strength Analysis of FPSO's Mooring Lines C.L.Siow, J.Koto, H.Yasukawa, A.Matsuda, D.Terada, C.Guedes Soares, Muhamad Zameri bin Mat Samad	161 - 166
Hydrothermal Synthesis of Hydroxyapatite From Cockle Shell Waste <i>Yelmida Azis, Zultiniar, Novesar Jamarun, Syukri Arief, Hadi Nur</i>	167 - 170

ISOMAse

International Society of Ocean, Mechanical and Aerospace -Scientists and Engineers-

Vol.1: 19-November 2014

About OMAse

The first Conference on Ocean, Mechanical and Aerospace for Scientists and Engineers is the conference organizes by International Society of Ocean, Mechanical and Aerospace – Scientists and Engineers – (ISOMAse).

The target for this conference is gathered the researchers involved in an area of ocean, mechanical and aerospace to share their findings and discuss the researches issue. We believe interchangeable of idea between researchers from ocean, mechanical and aerospace is important because all of the disciplines are sharing related sciences and engineering theories in their respect area. Therefore, we believe this conference will able to refresh the research experience of the people in these areas and generate impact for the cross discipline research collaboration and knowledge exchange.

ISOMAse

Vol.1: 19-November 2014

Scope of OMAse

The OMAse welcomes participants from academicians, scholars, and practitioners for possible publication from all over the world that meets the general criteria of significance and educational excellence. The scope of the conference is as follows:

- Environment and Safety
- Renewable Energy
- Naval Architecture and Offshore Engineering
- Computational and Experimental Mechanics
- Hydrodynamic and Aerodynamics
- Noise and Vibration
- Aeronautics and Satellite
- Engineering Materials and Corrosion
- Fluids Mechanics Engineering
- Stress and Structural Modeling
- Manufacturing and Industrial Engineering
- Robotics and Control
- Heat Transfer and Thermal
- Power Plant Engineering
- Risk and Reliability
- · Case studies and Critical reviews

The International Society of Ocean, Mechanical and Aerospace –science and engineering is inviting you to submit your manuscript(s) to isomase.org@gmail.com for the conference proceeding.

ISOMAse

Effect of Bending Angle Variation to the Strength of Steel Reinforcement Bar

Kana Sabatul Ikhwan, a,* and M. Dalil, a

1) Mechanical Engineering, Universitas Riau, Indonesia

*Corresponding author: ikhwan36@yandex.com

Paper History

Received: 11-September-2014 Accepted: 10-November-2014

ABSTRACT

One of reinforcement bar treatment during delivery transportation is to bend up or buckle in the middle of the bar. This treatment will undermine the strength of the reinforcement bar on buckle region due to its mechanical properties have been changed and no longer within specification. An important point of this study is to knowing the rate of change of mechanical properties, especially strength so that it can be given the appropriate safety factors in the use of steel reinforced concrete structure. Concrete reinforcing steel bent structure with nine variations of the bending angle starting from the angle (α) of 20° , 40° , 60° , 80° , 100° , 120° , 140° , 160° , and 180°. The maximum value of the yield strength and tensile strength in the range of maximum bending process is 662.9607 and 704.0271 MPa in bending angle of 160 degrees and 100 degrees.

KEY WORDS: Bending, Steel Structures, Mechanical Properties

NOMENCLATURE

A□ Initial Area (mm²) ΔL Length Increasing (mm)

- D Specimen Diameter (mm)
- E Modulus Of Elasticity (GPa)
- EL Elongation ductility (%)
- ε Strain
- F Tensile Force (N)
- σ Normal Stress (N/mm²)
- G Gauge Length (mm)

1.0 INTRODUCTION

Riau Province continues to accelerate infrastructure development is a key to spurring economic development in the communities in Lancang Kuning Earth. Especially the construction of physical facilities in Riau Province is currently rising very rapidly, such as the construction of office buildings, bridges, apartments, hotels, plazas, shops, and residential-housing community. Construction of the physical facilities require structural steel reinforcement as one of the main ingredients for reinforcing the strength of the concrete building. Concrete reinforcing steel structure production experience both the bending process for a particular purpose or other. One example is the bending of simplifying the transport of manufacturers in Jakarta or Medan to get to Pekanbaru Riau province or territory area through land transportation vehicles with a limited size (Shown in figure. 1).

-Science and Engineering-



Figure 1. Concrete reinforcing steel transportation (location; Pekanbaru)

There is also a reality in the field is not willful bending the current loading and unloading process and the reinforcing steel travel until it gets to the consumer. Most of the implementation of the concrete work in the field often encountered reuse of steel reinforcement has bent it.

2.0 LITERATURE REVIEW

Z.T. Zhang and S. J. Hu (1997) had been calculating stress and residual stress methods in plane strain bending. The influence of deformation theory and incremental theory, repeating bending, unbending andre-bending, cyclic material models and springback calculation methods on the stress or residual stressdistributions are examined and shown to be large ^[6].H.X. Zhu (2006) had been comparedthe deformation theory, theflow theory with either isotropic hardening or kinematic hardening, and the shell theory (which ignores the transverse stress. The solutions reveal that large curvature bending can result in asignificant thickness reduction of the bent plate, and therefore the non-dimensional bending moment initially increases with the non-dimensional bending curvature, reaches a peak point, and then drops with the further increment of the non-dimensional bendingcurvature^[8].

2.1 Concrete reinforcement steel structures

Steel reinforcement for concrete construction is shaped steel round bars and deep for building construction materials. The manufacturing process begins with the raw material is steel molds (ingot / billet) which has soothed (normalizing). The next is the process of hot rolled forming process is then performed (metal forming) is the process of withdrawal and stretching. Shown in Figure 1 following the formation process Ingots / Billets into bars:

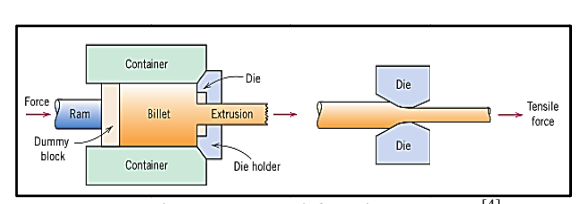


Figure 2. Metal forming process^[4]

Based SNI 03-2847-2002, type of concrete reinforcing steel in outline are available in the market there are 2 types, namely plain rebars (BJTP) and reinforcing steel screw or

fins (BJTs). Following the classification of plain concrete reinforcing steel in the market:

Table 1 Concrete Reinforcing Steel Size^[7]

1 4010	1. Concrete I	Nominal	Nominal	Nominal
No.	Nomination	Diameter	Area (A),	Weight/meter
		(D), mm	cm²	(kg/m)
1	P.6	6	0,2827	0,222
2	P.8	8	0,5027	0,395
3	P.10	10	0,7854	0,617
4	P.12	12	1,131	0,888
5	P.14	14	1,539	1,12
6	P.16	16	2,011	1,58
7	P.19	19	2,835	2,23
8	P.22	22	3,801	2,98
9	P.25	25	4,909	3,85
10	P.28	28	6,158	4,83
11	P.32	32	8,042	6,31

2.2 Air Bending

Air bending is the bending process where the punch presses the workpiece and there is no reason to hold the workpiece when the movement is continued until the maximum punch^[3]. There are two parameters, namely the bending angle alpha angle (α) and beta (β) as shown in Figure 2 below:

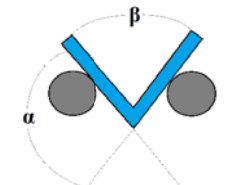


Figure 3. Bending angle parameters^[3]



Figure 4. Schematic stresses occur at the positive bending^[5]

When using a very sharp punch (compared to the sheetthickness), there is no need to explicitly model the contactbetween the sheet and the punch. It can be replaced byprescribed node displacement of the sheet in the vicinity ofthe symmetry axis^[3].

-Science and Engineering-

2.3 Mechanical Properties of Materials

Mechanical properties of a material is a parameter in the design of the basic information of a material and the strength of the supporting data for material specifications. Mechanical properties of a material obtained from a tensile test results give a bigger picture than other mechanical testing, which includes parameters yield stress (deformation), tensile strength, tensile strength, strain, elastic modulus, the percentage of the length, the percentage reduction in the size, toughness , plasticity, elasticity, plasticity, yield type, and shape of fracture experienced by the material.

2.4 Tensile Test

Tensile testing done to complete the design of the basic information of a material force. In tensile testing, the specimen is loaded coaxial tensile force that grew continuously. Along with the observations made regarding the extension experienced by the test specimen.

$$\sigma = \frac{F}{A} \tag{1}$$

$$\varepsilon = \frac{\Delta L}{L} = \frac{L - L}{L} \tag{2}$$

Dimensions of the test specimen (specimen) has been determined based on American Standard Testing and Material (ASTM) E8M that is shown in figure 5.

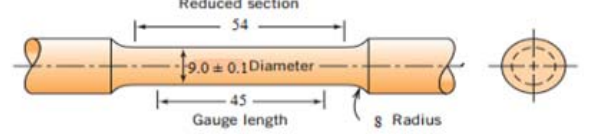


Figure 5. ASTM E8M^[1]

The data was first generated from tensile testing machine is a drag curve. Furthermore, from these data are converted into engineering stress strain curve (using equations 1 and 2). Engineering stress strain curve result from tensile test data can be to find some sort of mechanical properties, among others:

2.4.1. Strength

It is the response of a material to a force per cross-sectional area of the working force in which it is granted^[4]. Mechanical properties of tensile strength is further divided into three kinds of conditions based on engineering stress strain curve^[4], namely:

a. Yield Strength (Yield Strength)

That is occured at the beginning of the start of plastic deformation. The method of determining the yield strength is 0.002 distance of its strain and take the parallel line into the curve.

b.Maximum Tensile Strength

That is the maximum stress that occurs (curve peaks) in the engineering stress strain curve.

c. End Strength (Fracture Strength)

That last stress that occurs just before the specimen broke.

d. Modulus of elasticity

Elasticity is the ability of a material to return to its original shape when the applied force has been removed^[4]. The modulus of elasticity is the value of the stiffness of a material in which the proportional ratio between stress and strain in the elastic region in the stress-strain curve are characterized by the slope of the curve.

$$\mathsf{E} = \frac{\Delta \sigma}{\Delta \varepsilon} \tag{3}$$

c. Ductility (Ductility)

Ductility is a term to measure how much plastic deformation occurs until the material is dropped (Fracture)^[2]. In the tensile test, ductility measured in two ways:

1. Reduction of Area

$$\%RA = \left(\frac{A_o - A_f}{A_o}\right) x 100\% \tag{4}$$

2. Elongation

$$\%EL = \left(\frac{l_f - l_o}{l_o}\right) x 100\%$$
 (5)

3.0 METHODOLOGY

The methodology that used is experimental. The samples of material used is concrete reinforced steel structure production from PT. Krakatau Steel (indonesia) is known enough to have credibility in issuing a product with consistent specifications. Steel structures are widely sold in the city of Pekanbaru and used in a variety of building construction.

3.1 Grouping Sample of Testing

Performed with varying bending angle, it is starting from the point (α) of 20°, 40°, 60°, 80°, 100°, 120°, 140°, 160°, 180°, then straightened back and done testing to obtain tensile mechanical properties. The number of test specimens for each angle is not bent and bent test specimen is 5, so that for the test conditions are 45 test specimens. Specimen which is bent so that the amount of the 45 specimens, and are not bent as much as 5 specimens. Total Specimens for tensile test specimens was 50.

3.2 Research Procedures

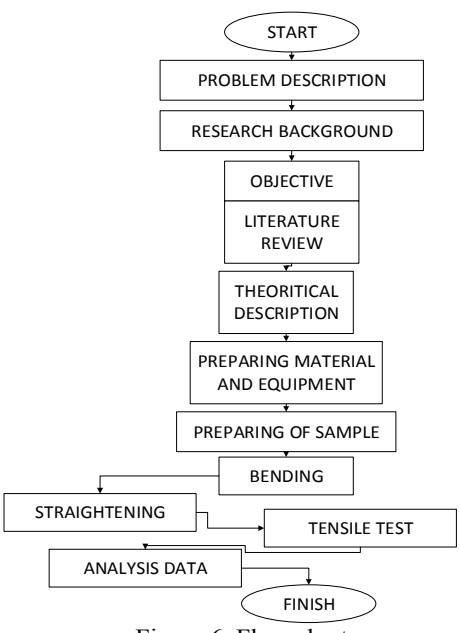


Figure 6. Flow chart

The first step is the process of cutting steel bars (12 mm of diameter) into 50 pieces. Once that is done the process of turning the central part of the specimen to be ASTM E8M (Shown in figure 7).



Figure. 7 Preparing of samples

The next is making holes on each end of the specimen to the laying of the retaining pin when the tensile test. Furthermore, the bending process is carried out with nine variations of the bending angle. After the bending process, then straightened out again with aligners. the results of the alignment is not perfect and this tends included in the sample treatment (Shown in figure 8).





Figure. 8 Bending and straightening

The curve resulting from tensile testing machine further processed to determine how much the yield strength and tensile strength.



Figure 9. Tensile Test

4. 0 RESULTS AND DISCUSSION

After a series of tensile tests on each specimen, the initial data are curves tensile testing. Tensile curve further converted into engineering stress vs. strain. The curve is then determined the value of the yield strength and tensile strength of the maximum value. Tensile test data as follows:

Table 2. Yield strength after bent for each spesimen

No.		В	ending Ang	le	
	0	20	40	60	80
Spec.	579.1983	618.7636	672.9798	528.1237	683.8457
Spec.	478.9057	575.4722	462.5709	636.0085	646.0013
Spec.	508.9326	596.4624	483.4772	535.5261	567.1252
Spec.	665.8346	592.1073	497.9339	550.8817	661.6460
Spec. 5	623.8377	438.2014	595.0918	637.1309	667.9474
Aver.	571.3418	564.2014	542.4107	577.5342	645.3131

-Science and Engineering-

Table.3: Yield strength after bent for each specimen (continued)

	Bendin	g angle (Co	ntinued)	
100	120	140	160	180
604.9335	640.3582	595.4814	684.3799	695.7560
647.3392	528.6524	592.3307	693.1530	678.7480
678.1649	594.7019	689.3138	702.1982	712.0572
607.2365	527.4709	657.1029	661.6460	586.0294
637.5983	582.9470	540.4405	573.4266	573.3576
635.0545	574.8261	614.9339	662.9607	649.1896

Tabel.4: Ultimate Tensile Strenght after bent for each specimen

No	Bending A	ingle			
No.	0	20	40	60	80
Spec.	693.8313	711.8786	702.0991	542.7938	702.6671
Spec.	537.5086	689.3678	471.5820	683.4201	703.8014
Spec.	544.3647	705.7154	537.1969	568.9965	573.4266
Spec.	727.4860	706.1658	534.3681	563.4018	727.8107
Spec. 5	712.0572	535.2317	637.5983	718.3339	683.7009
Aver.	643.0496	669.6719	576.5689	615.3892	678.2813

Table.5: Ultimate Tensile Strenght after bentfor each specimen (Continued)

Bending angle (continued)				
100	120	140	160	180
705.7558	683.0487	621.3171	726.7127	734.4091
723.7869	534.6598	607.4541	718.3586	742.0978
718.2383	732.4223	760.1779	724.7458	756.1669
704.3943	556.0163	708.6404	718.3586	595.4814
667.9601	640.6345	564.7299	611.2349	598.0181
704.0271	629.3563	652.4639	699.8821	685.2347

Data that has been averaged subsequently collected as shown in Table 2 as follow:

Table.6: Tensile strenght after bent

No.	Bending Angle (α)	Yield Strenght (Mpa)	Ultimate Tensile Strenght (Mpa)
-----	-------------------	-------------------------	------------------------------------

1	0	571.3418	643.0496
2	20	564.2014	669.6719
3	40	542.4107	576.5689
4	60	577.5342	615.3892
5	80	645.3131	678.2813
6	100	635.0545	704.0271
7	120	574.8261	629.3563
8	140	614.9339	652.4639
9	160	662.9607	699.8821
10	180	649.1896	685.2347

In these data can be seen that the yield strength and ultimate tensile strenght decreases in certain pembnegkokan corner and climb back on a certain bending angle. And then, the correlation between tensile strenght and bending angles as follows:

Strenght (Mpa)

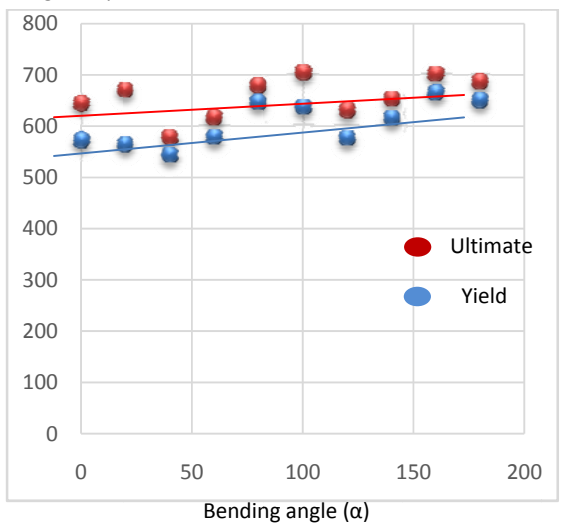


Figure.11: Strength vs Bending angle

Percentage the percentage is increased, and if the value is negative then decreased change in tensile strength at each bending angle can go up and can also go down. In table 7 is shown if the value is positive then

Table.7: Percentage change of mechanical properties

Bending Angle	Yield (%)	Ultimate(%)	Elongation (%)
0	0%	0%	24.67%
20	-1%	4%	22%
40	-5%	-10%	15%
60	1%	-4%	17%
80	13%	5%	21%
100	11%	9%	18%
120	1%	-2%	17%
140	8%	1%	19%
160	16%	9%	19%
180	14%	7%	13%

but with the increase in yield strength and ultimate strength, resulting in lower ductility due to strain hardening has occurred, as shown in the Figure 12 as follows:



Figure 12: Bending Angle vs Elongation

5.0 CONCLUSION

Based on tensile test data, it can be concluded that the yield strength and ultimate strenght impaired at an angle of 20 degrees bending and again increased at an angle of 80 degrees and 100 degrees, and again increased at an angle of 160 degrees to 180 degrees. The maximum value of the yield strength and tensile strength in the range of maximum bending process is 662.9607 and 704.0271 MPa in bending angle of 160 degrees and 100 degrees. The meximum decreased elongation is 11.67 % at bending angle 180 degrees. For the more result of accurate data should represent the number of samples multiplied.

REFERENCES

- 1. Annual Books of ASTM Standards. Metals Test Methods and Analytical Procedures. USA. Section Three, Volume 03.01. 1996.
- 2. Soboyejo, Wole, "Mechanical Properties of Engineered Materials". New York: Marcel Dekker, 2002
- 3. D. Reche, J. Besson, T. Sturel, X. Lemoine, A.F. Gourgues-Lorenzon a. *Analysis of the air-bending test using finite-element simulation Application to steel sheets.* MINES ParisTech, Centre des Mate 'riaux, CNRS UMR 7633, BP 87, 91003 Evry Cedex, France
- 4. William D. Callister, Jr., David G. Rethwisch, "Materials Science and Engineering", ISBN 978-0-470-41997-7
- Clifford, Michael, Richard Brooks, Alan Howe, Andrew Kennedy, Stewart McWilliam. 2009. An Introduction to Mechanical Engineering: Part 1. London: Hodder Education, An Hachette UK Company.
- 6. Z. T. Zhang, S. J. Hu. 1997. Stress and residual stress distributions in plane strain bending. Department of Mechanical Engineering and Applied Mechanics, University of Michigan, Ann Arbor, MI 48109, U.S.A.
- 7. SNI 03-2847-2002, SNI 07-2052-2002, Indonesian Standard of Concrete reinforcing steel structure.
- 8. H.X. Zhu. 2006. Large deformation pure bending of an elastic plastic power-law-hardening wide plate: Analysis and application. School of Engineering, Cardiff University, Cardiff CF24 OYF, UK

Study on Performance of Double Acting Tanker in Ice Condition

Efi Afrizal, a,c and Jaswar Koto, a,b,*

Paper History

Received: 10-October-2014 Accepted: 15-November-2014

ABSTRACT

An optimum procedure of hull form design for ice ship going "Double Acting Tanker" is introduced. The procedure orderly consist of hull form design, analyses of performance of a ship in open water and ice condition, maneuverability performance, ice loading effect on propeller and torsional shaft, and economical and environmental societies. In the present study, only two topics are mainly discussed, which are hull form design and then continued with performance analysis in ice condition and open water. For the hull form design the objective parameter are considered as follows; stem and the stern angles, upper and lower fore bulbous angles, entrance angles, and spreading angles. All those angles are investigated for both full loaded and ballast condition in ahead and astern. Special concern is needed for stern part due to existing propeller effect on ice breaking performance. The hull form is firstly investigated without installation of propeller to avoid the effect of pressure from propeller and then continued by installation of propeller to find the optimum propeller design and propeller immersion. Research in ice condition is compromised with open water. The optimum hull form, propeller design and propeller immersion is when the hull form gives better performance for both open water and ice condition. The selected hull form then is compared with existing DAT tanker "Tempera".

KEY WORDS: Double Acting Tanker; Ice Load; Ahead; Astern.

1.0 INTRODUCTION

The development of pod drive brought highly advantage of diesel electric power for improvement maneuvering capability and

icebreaking performance in astern mode during heavy ice condition for ice ship going. Application of pod drive on ship is firstly on icebreakers to have good capability to run astern. Combination of icebreaking and bulbous bow and pod drive brought possibility for a tanker to operate astern in ice condition and ahead in open water, which is called Double Acting Tanker "DAT" concept. Figure 1 to 2 shows Double Acting Tanker Tempera in open water and ice condition, respectively, which is built by Sumitomo Heavy Industries Japan.

The propulsion drive of the ship is provided by an Azipod unit, which contains the electric motor and the fixed pitch propeller. This is pod can rotate at 360o and has a maximum rating of 16 MWatt and the nominal output is 15 MWatt. This gives the tanker a speed of 15.2 knots in open water at 90 % of maximum continuous rating. In ice the tanker can go at 3 knots in 1 meter thick. The hull structure features a specially reinforced double skin with a fatigue life of 40 years. 1 This present study discusses and optimum procedure for optimization hull form for ice ship going "DAT". The performance of selected hull form design in ice condition and then is compared with the existing DAT "Tempera" from publishing data.



^{a)}Department of Aeronautics, Automotive and Ocean Engineering, Faculty of Mechanical Engineering, Universiti Teknologi Malaysia

b) Ocean and Aerospace Research Institute, Indonesia

c) Mechanical Engineering, Universitas Riau, Indonesia

^{*}Corresponding author: jaswar.koto@gmail.com

Figure 1: Double Acting Tanker Tempera in open water (1)



Figure 2: Double Acting Tanker Tempera in ice condition (1)

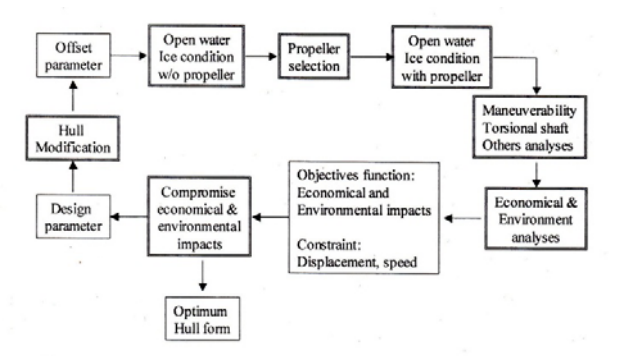


Figure 3: Hierarchy of optimization of hull form for ice ship going

2.0 OPTIMIZATION OF HULL FORM

A procedure for optimization of hull form for ice ship going is presented in (Fig. 1). The procedure mainly consist of hull form design, to open water, and ice condition performance with and without propeller, maneuverability, torsional shaft due to effect of ice loading and economical and environmental impacts on user and societies. The objective function are economic and environmental impact on user and societies. This means that the ship is selected based on satisfaction of user and societies. The viewpoint of user mean the ship owner view from profit and the societies viewpoint mean the local and international requirement such as regulation. This economic and environmental impact is investigated by using the economic and environmental model. Since the topic is constrain the present study only discusses the performance of hull form in open water and ice condition.

The constraint parameter in present study is 106000 ton of deadweight and 15.5 knot of speed. The optimization condition of hull form is designed to have capability to operate in both open water and ice condition in scantling and ballast draft. The fore part of vessel is fitted with bulbous bow as shown in (Fig. 2). The

bow shape is designed to be capable to operate in light ice condition. The modification of the fore profile is divided into three sections which is stern angle, upper and lower bulbous angles. The constrain of hull form design is as follows stem angle 55, upper bulbous angle 36.0-44.0 and lower bulbous angles 76.0-84.0, entrance angle at full loaded draft 54.0-64.0, entrance angle at ballast draft 26.0-38.0.

Modification of fore hull is shown in Figure 4. The hull is modified into two parts, which is upper part (α 1F and α 2F) for full loaded and lower part for ballast condition (α 3F).

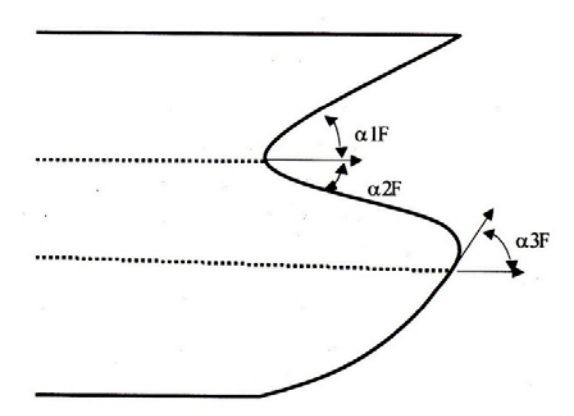


Figure 4: Two part of fore hull form modification.

Modification of hull form in the x direction can be expressed as where $X_{\sigma i}$ is station of parent hull form, X_{rml} is station of required hull form, X_1 is maximum station and X_0 is minimum station.

Then the modification of the hull form in the y direction can be expressed as where \mathcal{X}_{FL} is fixed station of the minimum point, and \mathcal{X}_{FU} is fixed station in the maximum point.

The modification of bulbous bow for ballast condition can be expressed as where z_{FL} is fixed waterline of minimum point and z_{FL} is fixed waterline of the maximum point.

The stern ice breaking type is designed to be able to operate independently in the most severe ice condition. After bulbous bow was modified similar to fore bulbous bow to reduce resistance as shown in Figure 5. The modification procedure of the stern part is same as the fore part.

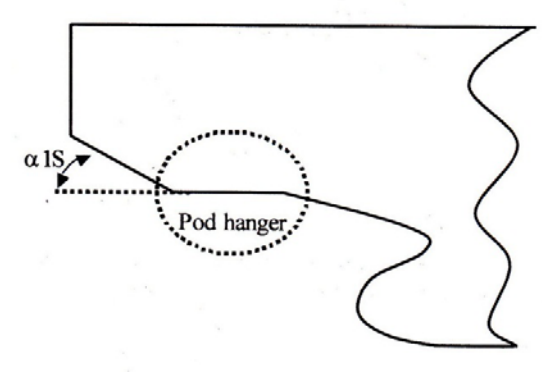


Figure 5: Stern part modification

3.0 PERFORMANCE ANALYSIS IN ICE CONDITION

The hull form of an ice ship going is analyzed in both open water and ice conditions. For each condition, the hull form is investigated with and without installing propeller. The investigation procedure is firstly start from fore part, and then continued to after part.

As the ship make an advanced progress to move forward into an unbroken ice field, the ship put forth sufficient amount of force to against the ice sheet. During the ice breaking process, two forces act on the same time, which are force given by the unbroken ice sheet and forced procedure by the ship. The force procedure by the ship can be classified into two component is procedure by thrust and vertical component provides ice breaking force.

The vertical force is incessantly transmitted to the ice sheet through the forward bow hull structure. When the vertical force and pressure go over in certain value, firstly, radial cracks propagate from loading point. Since loading of the ice continues, series of radial crack appear which as followed by one or more rows of circumferential cracks to ice failure. Then the ice failure is manifest in the formation of broken cusps or wedges. For the reason that the ship moves forward, the broken cusps become upended due to the hull flare. These cusps near the centerline of the ship and bow are simultaneously submerged and given a velocity that pass underneath the hull. In the case, the ship spend it force to against the submerging force from the ice cusps and frictional force between ice and hull.

The total acting force by the ice to resist the ship may be classified into four components, which are resistance for breaking and submerging ice, frictional ice hull, and loss momentum. The resistance can be expressed as

$$F_{ship} = F_{ise} + F_{sub} + F_{friet} + F_{moment} - F_{eff}, \qquad (1)$$

where; F_{fce} is resistance for breaking ice, F_{sub} is submersion resistance, F_{frec} is frictional resistance between ice and hull, $F_{brownent}$ is resistance due to loss momentum and F_{effect} is reduction resistance due to propeller effect, which is considered when the ship moves astern.

$$F_{toe} = C_1, \sigma, h^2, \mu, f(a, b)$$
 (2)

where; C_1 is an icebreaking coefficient, σ is ice flexural strength, h is ice thickness, μ is coefficient of kinetic friction of ice and hull and a, b are component angles fore or after parts

The submersion resistance is assumed arise from work required to tip and submerge the broken an ice cusps. The submersion resistance depends on buoyancy of force of the ice cusp due to different density between the ice cusp and seawater.

$$F_{\text{sub}} = C_2 \cdot (\rho_{\text{water}} - \rho_{\text{fee}}), g. D. B \tag{3}$$

where; C_2 is submersion coefficient, ρ_{mages} is water density 1.025 ton/m³, ρ_{fice} is ice density 0.918 ton/m³, ρ_{g} is acceleration of gravity 9.81 m/s², ρ_{g} is depth of ice cusp and ρ_{g} is width of the ice cusp.

The frictional resistance is developed when buoyancy force of the broken ice is against the hull and underside of the broken ice field as well as the effect of hull form such as friction between ice and hull and broken ice piece and under surface of the broken ice cover. The frictional resistance can be expressed as

$$F_{friet} = C_2, \rho_{loc}, g.r. h. B. V / f_{\overline{c}} f(a, b, C)$$
(4)

where; C_3 is frictional coefficient, L is ship length, C_W is water plane area coefficient of entrance part, V speed of ship in m/s.

Loss momentum resistance is developed when resistive force attributable to extract momentum from the ship and imparting it to broken ice pieces. The time rate of change momentum of the ship is equal to resultant force on ship, which can be expressed as

$$F_{\text{moment}} = C_4, \rho, B, h, V^2, f(a,$$
 (5)

The propeller effect is assumed due to pressure created from propeller which can be expressed as

$$F_{effect} = f(A_{W}, A_{J}, I_{Z}, 1) \tag{6}$$

where; A_W is working area, A_I is un-working area, I_F is propeller immersion and T_F is propeller thrust.

The principal dimension of ship which is evaluated in present study is shown in Table 1.

The fore and after part of ship are modified under constraint condition as follows: stem angle 55, upper bulbous angle 36.0-44.0 and lower bulbous angle 76.0-84.0 entrance angle at scantling draft 54.0-64.0 entrance angle at ballast draft 26.0-38.0. Propeller diameter is ranged from 7.4 to 7.6 m.

Table 1: Main principal dimension

Items	
Length, Lpp (m)	230
Beam (m)	44
Draft (m)	14.5
Deadweight (ton)	106100

Result of calculation are shown in Figure 6-13 in which Figure 6-9 show ice resistance of ship in full loaded and ballast draft in ahead without propeller, and Figure 10-13 show ice resistance of ship in fill loaded and ballast in astern without propeller. In figure w mean waterline angle and b mean bulbous angle at fore part and stern angle at stern part. The result show that resistance increase with increasing of entrance angle and bulbous angle. After compromising with open water condition and without propeller 36 and 54 degree are the suitable angle for upper bulbous and entrance angle at ballast draft, respectively and 76 and 28 degree are suitable for lower bulbous and entrance angle at ballast draft, respectively. For stern part 30 and 40 degree are

suitable for stern and stern angle for both full and ballast condition, respectively.

In order to evaluate hull form ice resistance by the selected hull form are compare with existing DAT tanker "Tempera" as shown in Figure 14-17. The result show that selected ship has lower ice resistance than Tempera in unfrozen and frozen channels in full load and ballast conditions.

Figure 6: Ice resistance in unfrozen channel at full loaded draft, ahead, H-ice: 1.0 m and Vs: 2.5 m/s

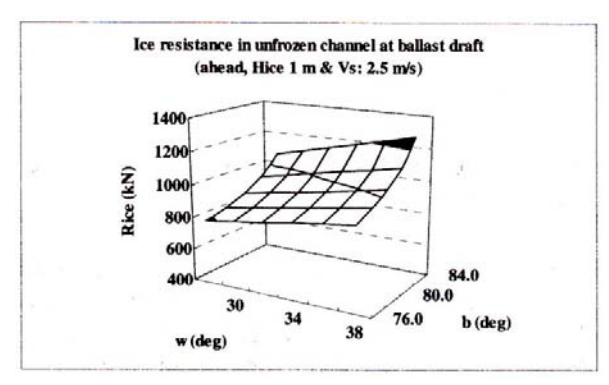


Figure 7: Ice resistance in unfrozen channel at ballast draft, ahead, H-ice: $1.0\ m$ and Vs: $2.5\ m/s$

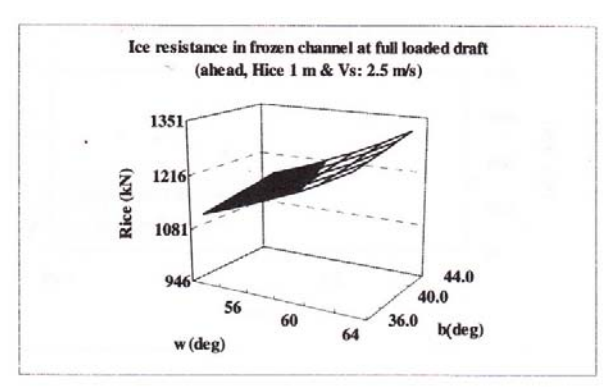
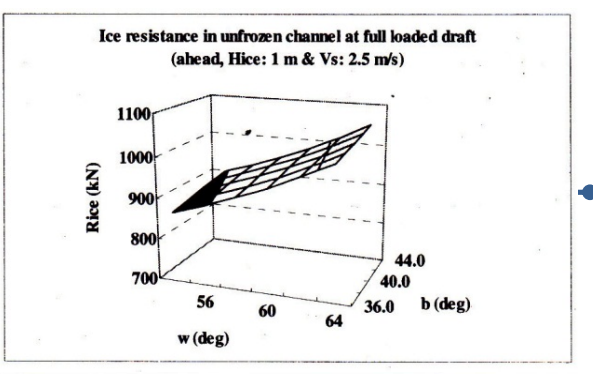


Figure 8: Ice resistance in frozen channel at full loaded draft, ahead, H-ice: 1.0 m and Vs: 2.5 m/s



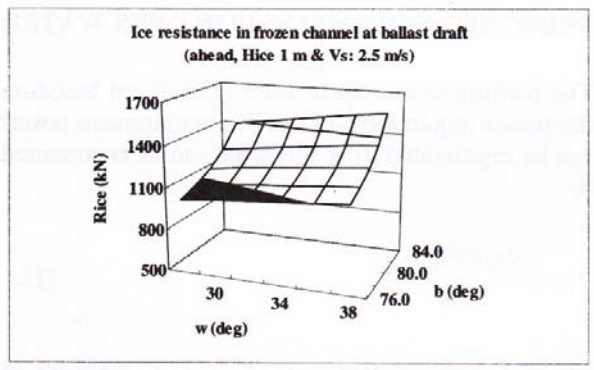


Figure 9: Ice resistance in frozen channel at ballast draft, ahead, H-ice: 1.0 m and Vs: 2.5 m/s

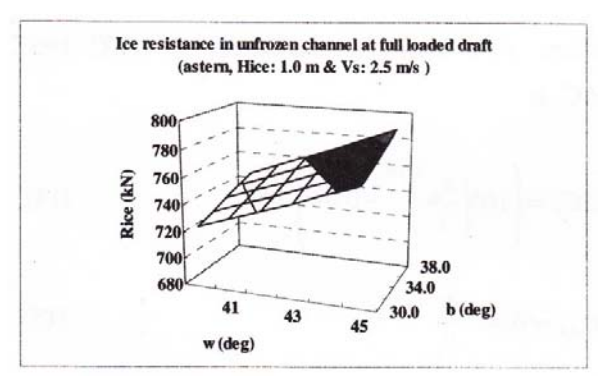


Figure 10: Ice resistance in unfrozen channel at full loaded draft, astern without propeller, H-ice: 1.0 m and Vs: 2.5 m/s.

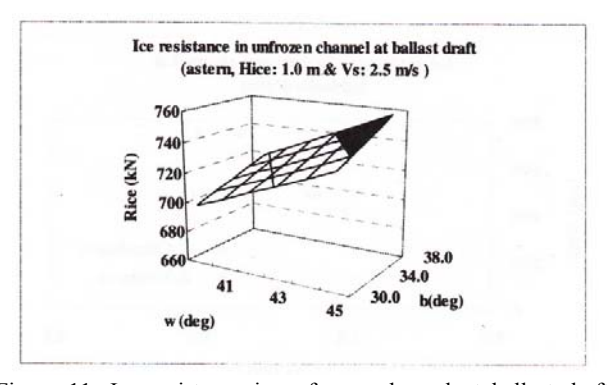


Figure 11: Ice resistance in unfrozen channel at ballast draft, astern without propeller, H-ice: $1.0\ m$ and Vs: $2.5\ m/s$.

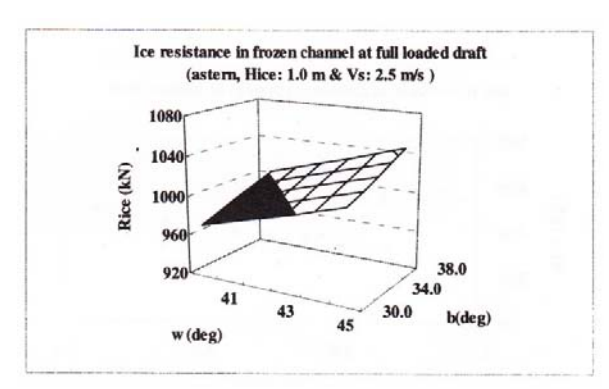


Figure 12: Ice resistance in frozen channel at full loaded draft, astern without propeller, H-ice: 1.0 m and Vs: 2.5 m/s

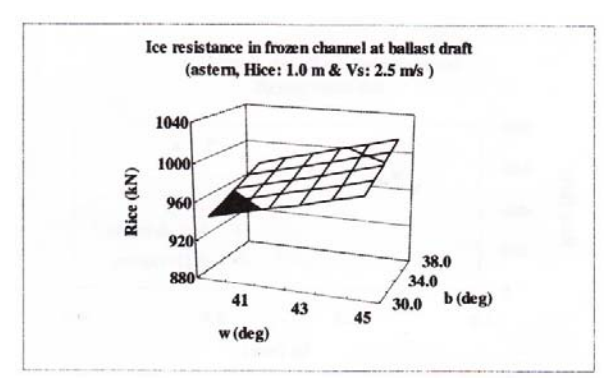


Figure 13: Ice resistance in frozen channel at ballast draft, astern without propeller, H-ice: 1.0 m and Vs: 2.5 m/s.

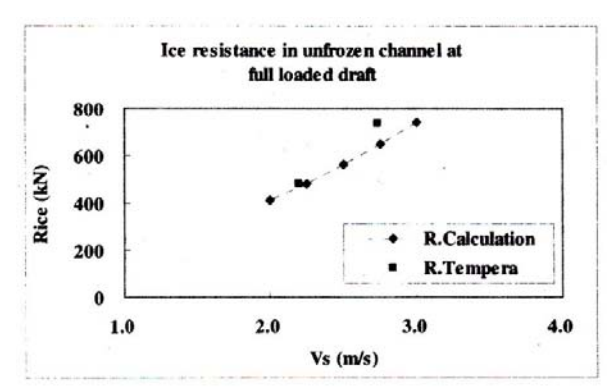


Figure 14: Comparison ice resistance of selected hull form in unfrozen channel at full loaded draft in astern with existing DAT "Tempera" (4)

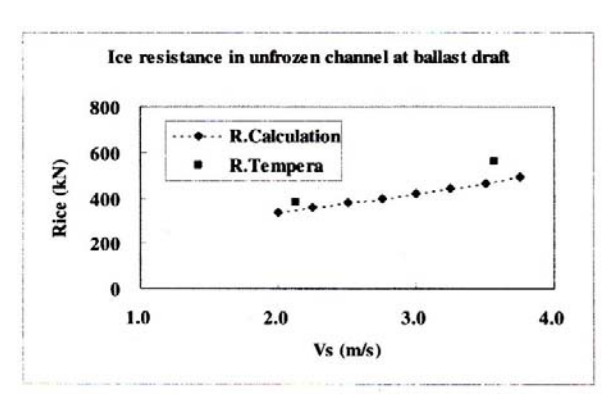


Figure 15: Comparison ice resistance of selected hull form in unfrozen channel at ballast draft in astern with existing DAT "Tempera" (4)

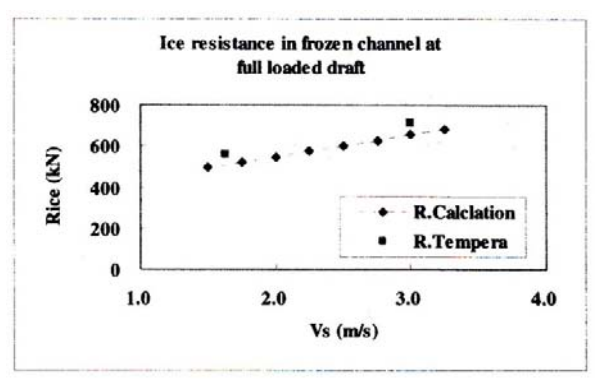


Figure 16: Comparison ice resistance of selected hull form in frozen channel at full loaded draft in astern with existing DAT "Tempera" (4)

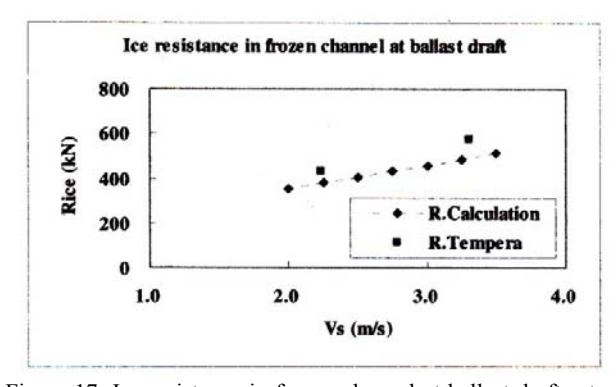


Figure 17: Ice resistance in frozen channel at ballast draft astern with propeller and then compare with existing DAT "Tempera" (4)

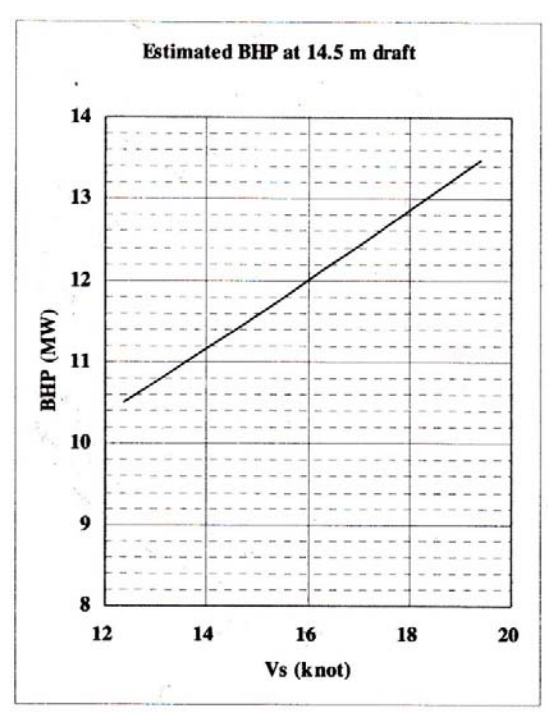


Figure 18: Estimated break horse power in open water of the selected ship

4.0 PERFORMANCE ANALYSIS IN OPEN WATER

The performance in open water is analyzed base on the power required by ship. The requirement power at the full scale can be represented by

$$P_{DS} = \frac{2\pi p D n_0 p_0}{n} \tag{7}$$

where seawater density (kg/m^3) , D is diameter of propeller, n_s is revolution per second, K_{ξ} torque coefficient and η relative rotate efficiency.

Total resistance in open water can be represented as

$$C_{\text{total}} = (1+k)C_f + \Delta C_f + C_W + C \tag{8}$$

where is frictional coefficient of ITTC 1957, \(\Delta\) is

$$\Delta C_f = \left[105 \left(\frac{m_Z}{r} \right) - 0.64 \right], 10^3$$
 $C_{AA} = 0.001 \frac{m_Z}{c}$

The estimated power curve of the selected hull form is shown in Figure 18.

4.0 CONCLUSION

The conclusions are obtained as follows: A method for optimization of hull for ice ship going is introduced. Using the method Double Acting Tanker is taken as a case study, and then

obtain result are compare with existing DAR "Tempera". The obtained result show that for fore hull form 36 and 54 degree are the suitable angle for upper bulbous and entrance angle at full loaded draft, respectively, and 76 and 28 degree are suitable angle for lower bulbous and entrance angle at ballast draft, respectively. For stern part 30 and 40 degree are suitable angle for stern and stern angle for both full and ballast condition respectively. The performance of selected hull form show better performance than existing DAT "Tempera" in ice condition such as unfrozen and frozen channels.

REFERENCES

- The Website for Cruise and http://www.ship-technology.com/
- Jaswar. 2002. A Prediction Method of Ice Breaking of an Icebreaker. Presented at Seminar of Applied Physic 2002. ITS Surabaya
- 3. Jaswar. Ikeda Y. 2002. A Feasibility Study of Double Acting Tanker Project Report Osaka Prefecture University and Sumitomo Heavy Industries. Japan.
- 4. Jaswar,
- Sasaki N., Laapio J., Fagerstrom B., Juurma K., and Wilkman G. 2005. Full Scale Performance of Double Acting Tanker "Tempera and Mastera". 1st International conference on Technology Advances in Podded Propulsion. UK.
- 6. Mewis F., 2001. *The efficiency of Pod Propulsion HADMAR* 22nd *International Conference*. Bulgaria.

Sound Source Localization by a Single Linear Moving Microphone

Meifal Rusli, a,* Lovely Son, Mulyadi Bur, and Agus Arisman, a

Paper History

Received: 25-October-2014 Accepted: 15-November-2014

ABSTRACT

This paper discusses about the implementation of a single microphone that is moving in linear track to substitute some channels of linear microphone array and a static microphone as a reference in beamforming method of sound source localization. The single microphone moves at constant velocity from a reference point. All recorded data from the moving and the reference microphone are split into several data represent each discrete microphone position. By this method, the sound localization system is modified from single microphone into artificial linear microphone array. Time delay for each artificial linear microphone is obtained by cross-correlation function between signal from moving microphone and signal from reference microphone. Time Domain beamforming method is performed by the delay-and-sum algorithm for stationary microphone. It is found that the methods can predict the direction of sound source. The shorter track and higher microphone speed can reduce the possibility of aliasing at high frequency sound. However, if the microphone moves closer to the sound source at higher speed, the possibility distortion of angle estimation increase caused by the Doppler effect. Furthermore, implementation of cross-correlation in beamforming can minimize the effect of random noise to predict the sound source direction.

KEY WORDS: Sound Source Localization; Time Domain Beamforming; Microphone Array; Moving Microphone

NOMENCLATURE

B	Number of beam
M	Number of Microphone
P(t)	Microphone Signal
$P_m(t)$	Beamforming Output Signal
Δ_m	Time Delay of Microphone Signal
	751 1

 ψ_b Direction angle w_m Weighting Function

1.0 INTRODUCTION

Sound source localization and visualization are complex task that most acoustics engineers face today. Some standard and highly functional methods based on microphone arrays are used throughout many industries to find and to analyze the noise source. In general, the methods fall into three categories: near-field acoustic holography, beamforming, and inverse methods. The methods were developed using some microphones and data acquisition channels. Most of them use 20 channel microphones or more.[1].

Beamforming is a process to perform spatial filtering, where the response of a sensors array is made sensitive to signals coming from a specific direction while signals from other directions are attenuated. Various methods of beamforming have been developed in time and frequency domain, depending on the processing speed and the signal types. Beamforming is typically referred to in SONAR [2] and RADAR [3]. Recently, its applications extend into seismic, medical ultrasonic imaging, and various other applications [4].

The beamforming technique was first developed for submarines and environmental applications. In the far field, sound waves hitting the microphone array are planar waves. Under these conditions, it is possible to propagate the measured sound field directly to the test object. All microphone signals measured by the

^{a)}Mechanical Engineering Department, Faculty of Engineering, Andalas University, Padang 25163-Indonesia

^{*}Corresponding author: meifal@ft.unand.ac.id

beamforming array are added together, taking into account the delay corresponding to the propagation distance. The pressure can be calculated at any point in front of the array, allowing propagation to any kind of surface. Beamforming is sometimes called "sum and delay," since it considers the relative delay of sound waves reaching different microphone positions. Beamforming requires that all data be measured simultaneously. It is typically done with a measurement system of 40 channels or more [1].

Recently, sound source localization by beamforming has been addressed to the problem of tracking moving sources [5-6]. This paper will discuss the implementation of a single microphone that is moving in linear track to substitute some channels of linear microphone array. The signal from moving microphone is compared with a static microphone as reference signal. Beamforming is performed using cross-correlation function between signal from moving microphone and reference signal from static microphone.

2.0 TIME DOMAIN BEAMFORMING ON MOVING MICROPHONE

The visualization of sound sources on arbitrary objects can be of great utility to locate, compare and demonstrate the causes of noise. To do so, an object can be modeled by placing a grid of hypothetical point monopoles on its surface. Focusing each of these sources by running a beamforming algorithm on measurements done with a microphone array, the influence of a source to the overall noise can be determined. To replace microphone array, a moving microphone and a static reference microphone is possibly developed. The idea is inspired by implementation of a moving subject like robot to identify or localize sound source objects. As preliminary research, we focus on locating the sound sources by adapting a classic time-domain beamforming method.

2.1. Beamforming On Static Microphone Array

The approach used in this paper is based on delay-and-sum beamforming that assuming point monopoles and spherical wave propagation. The beamformers output signal p(t) is obtained by [6]

$$p(t) = \frac{1}{M} \sum_{m=1}^{M} w_m p_m \left(t + \Delta_m \right)$$
(1)

That is summation of M microphone signals $p_m(t)$ after each of them is delayed by the time Δ_m and weighted by the factor w_m . The delay times, are usually calculated with

$$\Delta_m = \Delta t_{nm} - \Delta t_{n0} \tag{2}$$

where Δt_{nm} is the sound propagation time between source and microphone and Δt_{n0} is a reference time between the source and the array center. Because Δt_{n0} is equal for all microphone signals it only changes the absolute time frame of the output signal. This is irrelevant for most evaluations that can be run on the output

signal, so this offset can be neglected. The weighting factors, that assure that all microphones have the same impact on the result no matter how far away they are from the source, are calculated with

$$w_m = \frac{r_{nm}}{r_{n0}} \tag{3}$$

Im many cases, spatial weighting function w_m is defined as a window function to control main-lobe width and side-lobe magnitude.

To form a beam in direction ψ_b , the discrete delay required to bring the output of the M sensors into time alignment is equal to q_{mb} , which are integer multiplies of the sample spacing t_s , if the beam index b, is an integer ($b=0, \pm 1, \pm 2, \pm 3, \ldots$) then the beam directions that we can realize are those for which

$$\Delta t_{nm} \sin \psi_b = b \tag{4}$$

and effectively quantizes the beam steering directions ψ_b , such that

$$\psi_b = \sin^{-1}(b \cdot \frac{1}{\Delta t_{\text{min}}}) \tag{5}$$

2.2. Beamforming On Moving Microphone

When a fixed source is measured with a moving microphone over a period of time, the distance between source and microphone is no longer constant, but as a function of time. Figure 1 shows the consequences this has on phase and amplitude of the recorded signal by taking two events that take place when moving microphone is approaching source at the times t_1 and t_2 and observe how the sound propagates through the fixed medium to the microphone. Because the sound emitted at t_2 needs less time to reach the microphone than the signal emitted at t_1 , the waveform between these events is compressed resulting in an increase of frequency known as the Doppler Effect [6]. Likewise, because the distance decreases, the amplitude increases over time. Conversely, when the microphone moves away from the sound source, the sound emitted at t_2 needs more time to reach the microphone than the signal emitted at t_1 , the waveform between these events is expanded resulting in a decrease of frequency.

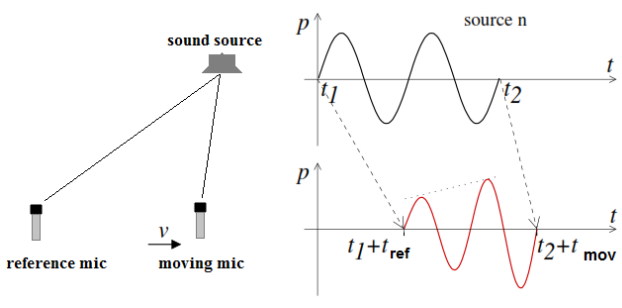


Figure 1. Doppler's effect when microphone moves closer to the sound source

In the case of moving microphone, two microphones are implemented to record the signals. One microphone in static position acts as reference signal, and another one moves in linear track with a constant speed. Both microphones record the signal in a same time, and have the same dimensions. Both signal then are divided in accordance with the desired number or microphone

distance of artificial microphones arrays of beamforming to substitute some channels of linear microphone array. Delay time of each artificial microphone array is obtained from crosscorrelation of the signal from moving microphone and the signal from reference microphone at the same time measurement. Then, beamforming is performed by cross-correlation function between signal from moving microphone and reference.

A simple time domain beamforming structure is the delayand-sum beamformer which implements in Equation (1) and is shown in Figure 2. The structure is repeated B times, where B is the number of beams desired. The cross-correlation signals are converted to a digital signal at a frequency greater than the Nyquist rate to achieve acceptable beam pattern performance. The signals are then delayed appropriately and the weighting function applied and effectively summed. If same set of weights are to be used for all steering directions, as is often the case, the weights can be applied directly at the sensor outputs, before the delay sum operation.

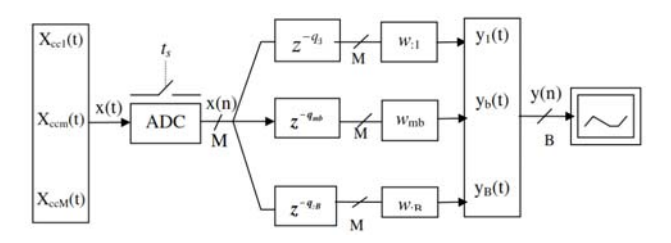


Figure 2. A simple Time domain-Delay sum beamformer using cross-correlation signal

3.0. RESULT AND DISCUSSION

Simulation is performed using configuration shown in Figure 3. The reference microphone is set at the beginning of the track, and the moving microphone moves on the microphone track with a constant speed. First, Microphone track is 2 meters length and sound source is allocated at 1 meter from the center of microphone track in x-axis and 4 meters in y-axis. It means that the sound source position is equal to $\tan^{-1}(4/1) = 75.9^{\circ}$ from x-axis of microphone track. Noise source is set in coordinate (4 meter,4 meter) from the center of the microphone track.

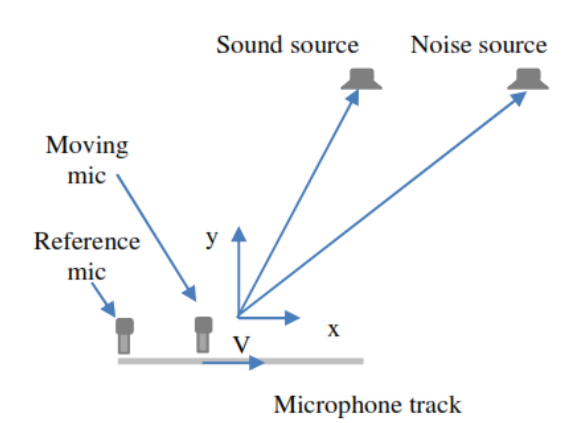


Figure 3. Simulation configuration

First, The simulation is performed with a single sound source and without noise. The beamforming is applied to predict the sound location i.e sound source direction from the center of microphone track with variation of sound frequency and microphone speed. Artificial array is set 1 cm of microphone distance, and frequency signal is varied from 500 to 4000 Hz.

When moving microphone moves at 1 m/s, beamforming is able to detect the position of sound source at 75° at frequency from 500 Hz to 1000 Hz (Figure 4). However aliasing occurs at frequency 2000 Hz or more, where total time delay between artificial microphones along the track is more than a wave length of the sound.

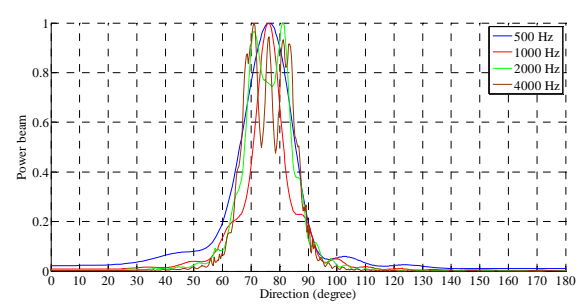


Figure 4. Beam power with microphone speed 1 m/s and 2 meters track length

When the microphone moves at 5 m/s of speed (Figure 5), beamforming is able to detect the sound source at frequency up to 2000 Hz. Aliasing still occurs at frequency 4000 Hz. However, the location prediction is shifted to lower than 75°. It is possibly caused by the Doppler's effect where the frequency and phase is changed when microphone move closer to the sound source in higher speed. Position estimation at higher frequency is distorted to the lower angle of direction.

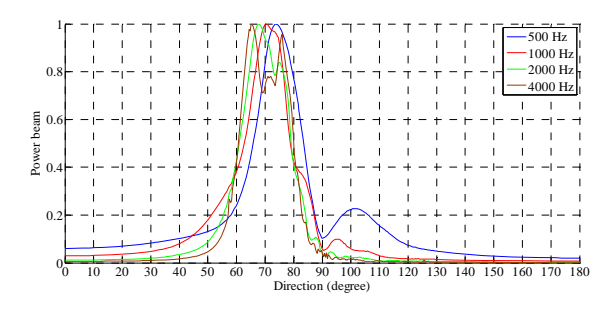


Figure 5. Beam power with microphone speed 5 m/s and 2 meters track length

Furthermore, when the microphone moves at 10 m/s speed (Figure 6), beamforming is able to detect the sound source at frequency up to 2000 Hz. Aliasing still occurs at frequency 4000 Hz. However, the location prediction is shifted to the bigger angle more than 75°. It is same with the previous situation, the doppler's effect causes frequency and phase change when microphone move closer to the sound source at higher speed.

Position estimation at higher frequency is distorted to lower angle of direction

The second condition is the microphone track has 0.5 meters length and sound source is allocated at 1 meter from the center of microphone track in x-axis and 4 meters in y-axis. It means that the sound source position is equal to $\tan^{-1}(4/1) = 75.9^{\circ}$ from x-axis of microphone track. Artificial array is set 1 cm of microphone distance, and frequency signal is varied from 500 to 4000 Hz.

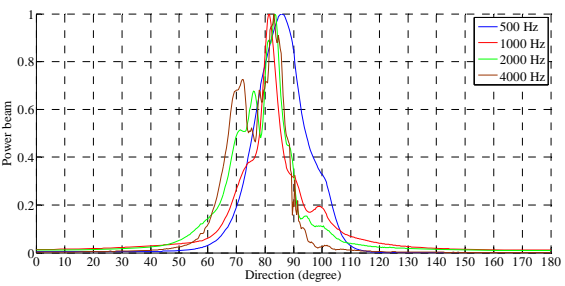


Figure 6: Beam power with microphone speed 10 m/s and 2 meters track length

When the microphone moves at 1 m/s, beamforming is able to detect the position of sound source at 73⁰ - 74⁰ at frequency from 500 Hz to 4000 Hz (Figure 7), without any aliasing. The same condition occurs when the microphone speed is 5 m/s (Figure 8). However, estimation of direction at frequency signal is shifted to higher angle. On the other hand, when microphone speed is 10 m/s (Figure 9), the direction of sound source with higher frequency is able to be estimated well. However, signal at lower frequency is predicted at higher angle.

Above explanation shows that shorter track and higher microphone speed can reduce the possibility of aliasing even. However, higher speed of microphone increases the possibility distortion of angle estimation caused by the Doppler's effect.

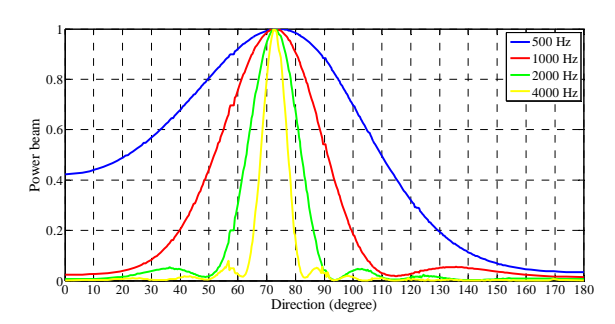


Figure 7. Beam power with microphone speed 1 m/s and 0.5 meters track length

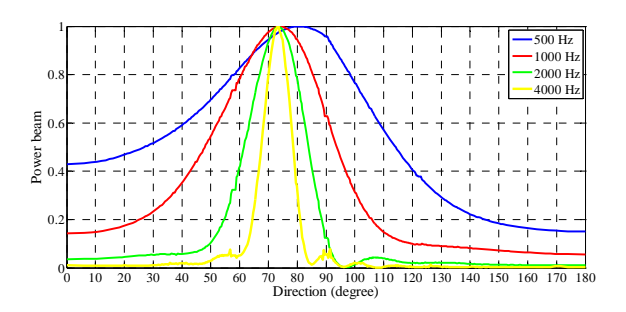


Figure 8: Beam power with microphone speed 5 m/s and 0.5 meters track length

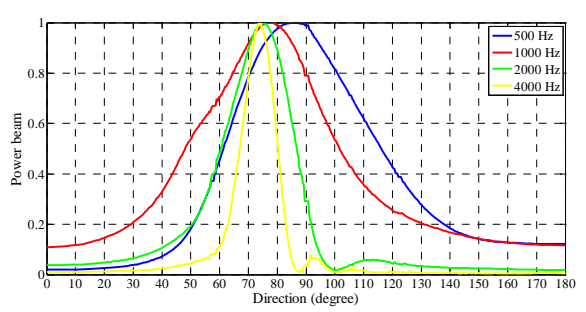


Figure 9: Beam power with microphone speed 10 m/s and 0.5 meters track length

Next, the random noise is applied to the system. Signal to noise ratio (S/N) is varied from 8 to 0.125. Figure 10 shows the example of the signals generated by sound source and noise source. As a result, Figure 11 shows, when sound signal at frequency 1000 Hz and microphone moves on 2 meters track length at 1 m/s and 2 m/s microphone speed, beamforming is able detect the sound location although S/N ratio reach 8 (Figure 11 and Figure 12)

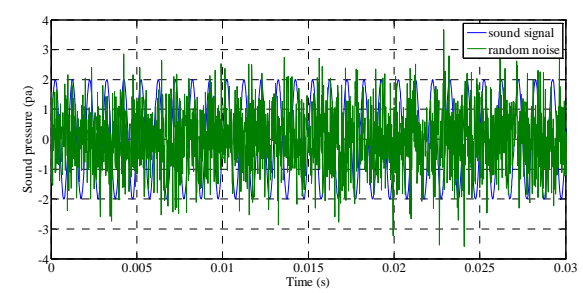


Figure 10: Sound and noise signal with S/N 0.5

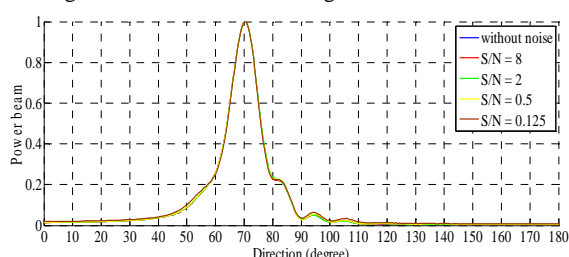


Figure 11: Beamforming of 1000 Hz signal, microphone speed 2 m/s with some levels of noise

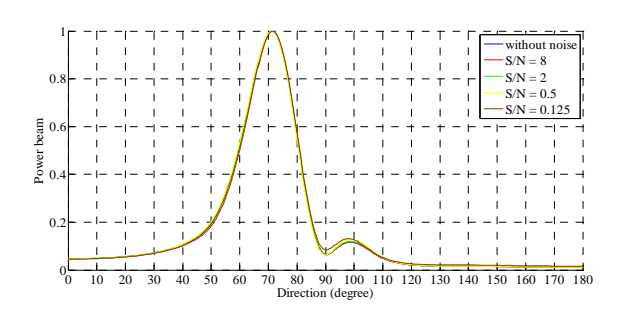


Figure 12: Beamforming of 1000 Hz signal, microphone speed 5 m/s with some levels of noise

The implementation of cross-correlation in beamforming can minimize the effect of random noise to predict the sound source direction.

4.0. CONCLUSSION

This paper has discussed about the implementation of a single moving microphone and another static microphone acts as reference in sound source localization. By this method the sound localization system is modified from single microphone into artificial time delayed linear microphone array. Time delay for each artificial time delayed linear microphone array is obtained from cross-correlation between signal moving microphone and signal from reference static microphone. The Time Domain beamforming method for moving sources of sound is performed by the delay-and-sum algorithm for stationary microphone. It is found that the methods can predict the direction of sound source. The shorter track and higher microphone speed can reduce the possibility of aliasing even at high frequency sound. However, higher speed of microphone increases the possibility distortion of angle estimation by the Doppler's effect. Furthermore, implementation of cross-correlation in beamforming can minimize the effect of random noise to predict the sound source direction.

ACKNOWLEDGEMENTS

This paper is part of the research funded by Hibah Fundamental of BOPTN - Andalas University by contract number 07/UN.16/PL/D-FD/2014. The authors gratefully acknowledge for this financial support.

REFERENCE

- Lanslots, J., Deblawe, F. Janssens, K. (2010). Selecting Sound Source Localization Techniques for Industrial Applications, Sound & Vibration, June 2010, pp.6-9
- Curtis T. and Ward R., "Digital beamforming for SONAR systems", IEE Proceedings, vol. 127, August 1980
- 3. Barton P., (1980) "Digital beamforming for RADAR", IEE Proceedings, vol. 127, August 1980

- 4. Donnell M. O., "Applications of VLSI circuits to medical imaging", Proceedings of the IEEE, vol. 76 September 1988.
- Zechel, g., zeibig, a. Beitelschmidt, m., Time-Domain Beamforming On Moving Objects With Known Trajectories, 3rd Berlin Beamforming Conference, 24-25 February 2010
- Ginn, B., Gomes, J., Hald, J. Recent advances in Rail Vehicle Moving Source Beamforming, Internoise, 15-18 September 2013, Innsbrug-Austria

Performance of Air Conditioning Water Heater with Trombone Coil Type as Dummy Condenser at Different Cooling Loads

Azridjal Aziz, a,* and Arya Bhima Satria, a

^{a)}Thermal Engineering Laboratory, Mechanical Engineering Department, University of Riau, Indonesia

*Corresponding author: azridjal@yahoo.com

Paper History

Received: 9-November-2014 Accepted: 15-November-2014

ABSTRACT

This paper presents the experimental performance study to observe the effect of changes in the cooling load of the combined air conditioning and water heating system with trombone coil type as dummy condenser using heat wasted from split type air conditioner. Effects of the following parameters to the system performance were examined: compressor power test chamber, test chamber temperature, condenser temperature, hot water temperature and Coefficient of Performance (COP). The results showed that the bigger the cooling load is given in the test chamber, the bigger the heat absorbed in the evaporator, so the higher the temperature of the hot water in a tank. COP increased with increasing of cooling loads. It was concluded that by combined air conditioning and water heating system so that space cooling and water heating can take place simultaneously, and the energy performance can be raised considerably.

KEY WORDS: air conditioning, water heater, cooling load, COP, compressor power

NOMENCLATURE

COP Coefficient of Performance

P Pressure T Temperature

COP Coefficient of Performance COP_R COP Refrigeration

COP_{R+HP} COP Refrigeration and Heat Pump

1.0 INTRODUCTION

The need of hot water is usually obtained from the electricity and gas that requires considerable energy, with energy recovery of waste heat from condenser in the air conditioning will be saving considerable energy. In thermodynamics terms of balance of energy, the waste energy from the condenser are combination of compressor energy and cooling effect energy in the evaporator, which means that energy wasted in the condenser is big enough, so that the potential of energy savings from condenser also big.

The electrical energy saving for water heating purposes by use the waste heat energy from the condenser also indirectly will save the use of fuel oil. The efficient uses of fuel as an energy source for the generation of electrical energy will have a positive impact on the environment, so that the recovery of energy from waste heat condenser using condenser dummy will give positive impact to the environment. The use of AC with the addition of a dummy condenser for water heating will save the cost of using electrical energy or gas because the cost of water heating from the condenser dummy obtained free of charge without increasing the cost of the use of AC. With the use of a dummy condenser at the AC will get two benefits at once that the rooms were comfortable and the hot water for various purposes.

Air conditioning water heater operates on an electrically driven vapor-compression cycle and pumps energy from the air in its surroundings to water in a storage tank, thus raising the temperature of the water. Air conditioning water heater are a promising technology in both residential and commercial applications due to both improved efficiency and air conditioning benefits. The super-heated refrigerant from compressor discharge of the air-conditioning system passes through a dummy condenser as trombone coil heat exchanger thereby transferring its heat to the cold inlet water within water heater tank. From this heat recovery technology, free hot water is produced in cooling operation, will achieve the highest COP. The temperature of the refrigerant is reduced, resulting in the two benefit of water heating and cooling. for higher air conditioning energy efficient.

Many researcher have been performed on heat pump water heaters (HPWHs), including structure, thermodynamics, working fluids, operation controlling, numerical simulation economical analysis (Jie Ji et al. 2003, Fei Liu et al. 2008, M. M. Rahman et al. .2007, M. Joseph Stalin et al. 2012, Jie Ji et al. 2005, U. V. Kongre et al. 2013, Arif Hepbasli, 2009). Sreejith K, 2013 was investigated experimentally the effect of different types of compressor oil in a domestic refrigerator having water cooled condenser and the recovered heat from the condenser can be used for bathing, cleaning, laundry, dish washing etc. Yi Xiaowen and W.L. Lee, 2008 have been reported an experimental study on the performance of a domestic Water-cooled Air conditioner (WAC) using tube-in-tube helical heat Exchanger for preheating of domestic hot water. Mehmet Yilmaz, 2003 has been presented the performance analysis of an air-to-water vapor compression heat pump system using pure refrigerants and zeotropic refrigerant mixtures.

Main objectives of this study were to investigate experimentally the combined air conditioning and water heating system using R22 as working fluid. Effects of the following parameters to the system performance were examined: compressor power test chamber, test chamber temperature, condenser temperature, hot water temperature and Coefficient of Performance (COP).

2.0 EXPERIMENTS

2.1 Experimental Apparatus

In this study, performance investigation is conducted using the similar experimental apparatus as described in Azridjal et al, 2014. As seen in Figure 1, the apparatus has the air conditioning system with a nominal capacity 2.6 kW. and water cooled dummy condenser with trombone coil type heat exchanger (Figure 2). Since Azridial et al. 2014 contains all the details of the test apparatus, measurements, test procedures, data verification etc., an interested reader is referred to Azridjal et al. 2014. In this paper test procedure will be described.

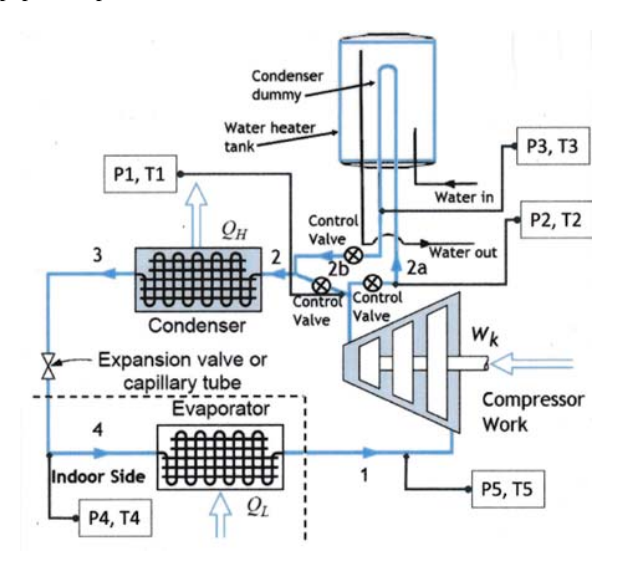


Figure 1: Schematic of Air Conditioning Water Heater (Sonntag, 2009, Azridjal et al.2014).



Figure 2: Condenser dummy trombone coil type

The schematic diagram of air conditioning water heater system is shown in Figure 1. The system can offer the following two operating modes. Mode 1 is only for space-cooling mode, this mode is like the common air-conditioning circles. Mode 2 can act as space-cooling and water heating mode. The switching among two modes is by means of on-off controls of the control valves valve. In this study, air conditioning water heater was operated in mode 2.

2.2 Test Procedure

Test procedure is as follows:

- 1. Ensure the apparatus is in good condition and there is no leakage of refrigerant.
- 2. Ensure that all test equipment is mounted properly.
- 3. The apparatus is turned on by connecting power cord to a electric current source and turn on the evaporator in a test chamber with set up temperature 16 °C.
- 4. Data were taken every 5 minutes for 120 minutes. Data collection depends on the parameters such as temperature, pressure, electric current, voltage in four condition: without load, and with load from electric bulb (1000 W, 2000 W and 3000 W)
- 5. When data recording were finished, turn off the apparatus in the test room and unplug the power cord from the current

3.0 RESULT AND DISCUSSION

Based on the design that has been done, the result of design the dummy condenser as heat exchanger is used type of trombone coil as shown in Figure 2. The trombone coil pipe was made of using a 3/8 inch diameter copper pipe, with 5 windings and 5,338 meters length. Then, the dummy condenser is placed in the water tank, which has a volume of 50 L that will be used for water heating. This heater is installed after the compressor and before the condenser, as shown in Figure 1.

Figure 3 shows the compressor power for two operation of system in different cooling load using dummy condenser. The testing of air conditioning water heater in mode 2, when the cooling load increase in the test room, the compressor power will increase too. This is because the heat that absorbed by the evaporator increase with increasing of cooling load and it will cause compression power increase. It is affected by the heat which absorbed by the refrigerant in the evaporator increase, so compression power also increase. Compressor power average at loads of 3000 watts is 0,74526 kW, while without loads is 0,57635 kW, it appears that compressor power increasing that tends to occur linearly.

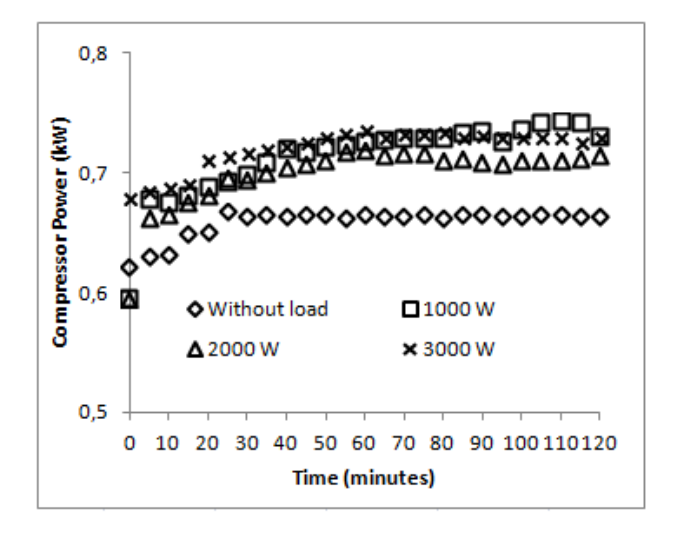


Figure 3: Compressor power vs. time at different cooling loads using dummy condenser

Figure 4 shows the distribution of water temperature in tank at different cooling load using dummy condenser. The higher cooling load is given in test chamber, the higher temperature of the water produced. This is because due to the heat generated by the condenser higher when the cooling load in the test room increase. The bigger cooling load given in the test room, the bigger heat absorbed in the evaporator, so the greater heat rejected in the dummy condenser that will heat the water in the tank. Where the highest water temperature at cooling loads 3000 W is 64.33 0 C, while without load is 61.54 0 C.

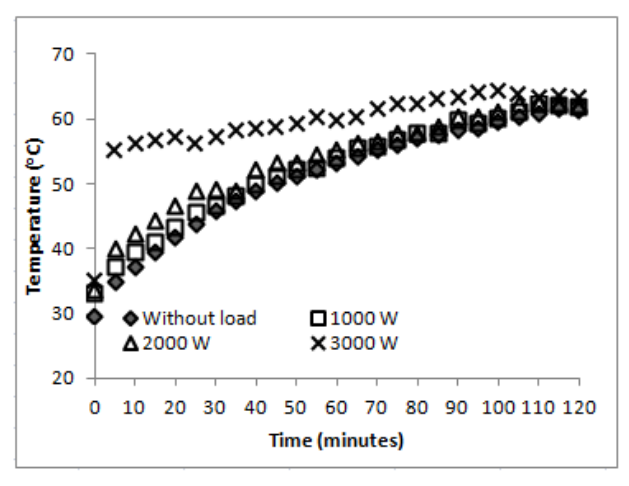


Figure 4: Water temperature in a tank vs. time at different

cooling loads using dummy condenser

Figure 5 shows condenser temperature and test room temperature at different cooling loads . At different cooling loads during 120 minutes of testing, it appears that the temperature of the condenser and temperature of test room tend toward steady condition after 30 minutes of testing. Condenser temperature and the temperature of the test room tend to rise with the increasing amount of cooling load, this is because the heat from the cooling load will be absorbed in the evaporator increase, so that the bigger the heat is removed in the condenser. The average temperature of the condenser at without load condition, 1000 W loads, 2000 W loads and 3000 W loads respectively are 72.66 $^{\circ}$ C, 70.07 $^{\circ}$ C, 76.72 $^{\circ}$ C and 78.12 $^{\circ}$ C. While the average temperature of the test room without load condition, 1000 W loads, 2000 W loads and 3000 W loads respectively are 20 $^{\circ}$ C, 18.03 $^{\circ}$ C, 22.57 $^{\circ}$ C and 26.09 $^{\circ}$ C.

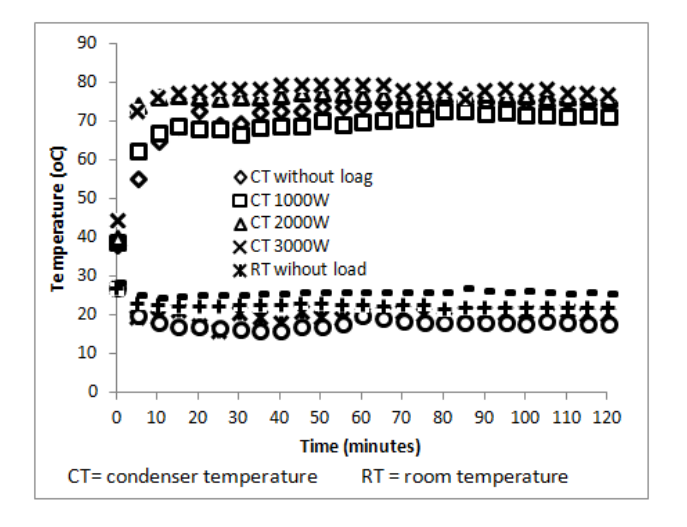


Figure 5: Condenser Temperature and test room temperature at different cooling loads

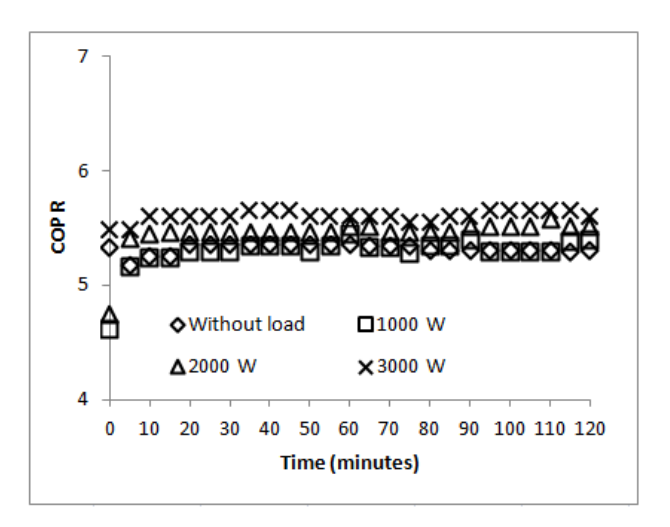


Figure 6: Coefficient of Performance Refrigeration (COP_R) vs. time at different cooling load using dummy condenser

Experimental results of Coefficient of Performance Refrigeration (COP_R) vs. time at different cooling load using dummy condenser is shown in Figure 6. As shown in Figure 6, the increase of cooling loads causes that the COP_R increases. The average COP_R of system without load condition, 1000 W loads, 2000 W loads and 3000 W loads respectively are 5.31, 5.33, 5.48 and 5.62.As seen in Figure 6, because compressor power increases with the rise of cooling load. Increasing the cooling load in the test room also will increase COP_R because the cooling power to be supplied at the evaporator increase too.

Coefficient Performance of Refrigeration and Heat Pump (COP_{R+HP}) as air conditioning and water heater at the different cooling load is shown in Figure 7. As the cooling load increases in the test room, COP_{R+HP} also increasing, although in cooling load 2000 W some time a little higher than 3000 W. The performance of COP_{R+HP} is bigger than COP_{R} because the benefits of cooling and heating are used simultaneously. Dummy condenser plays an important role in achieving higher system performance. Coefficient of Performance is higher for the combined system as air conditioning and water heater with dummy condenser. The use of dummy condenser as trombone heat exchanger affects the COP and the value of the optimum work compressor as shown in Figure 3.

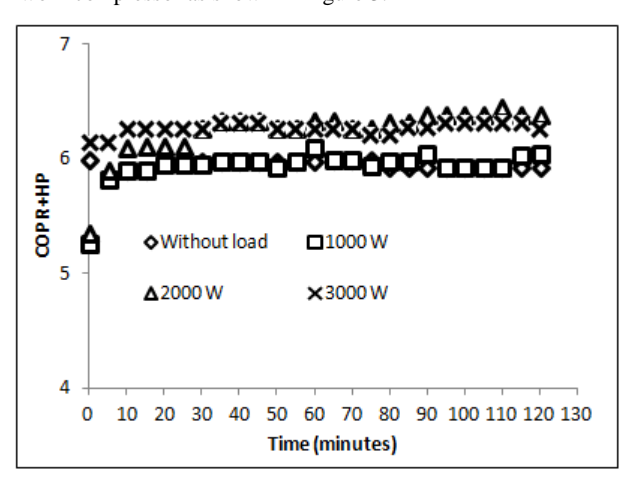


Figure 7: Coefficient of Performance Refrigeration and Heat Pump (COP_{R+HP}) vs. time at different cooling load using dummy condenser

4.0 CONCLUSION

The experimental performance study to observe the effect of changes in the cooling load of the combined air conditioning and water heating system using heat wasted from split type air conditioner are presented. The results indicate that the higher the cooling load is given in the test chamber, the greater the heat absorbed in the evaporator, so the higher the temperature of the hot water produced in the hot water tank. When the cooling load increase the COP_R and COP_{R+HP} also increasing too as the benefits of cooling and heating are used simultaneously. It was

concluded that by combined air conditioning and water heating system so that space cooling and water heating can take place simultaneously, the energy performance can be raised considerably.

ACKNOWLEDGEMENTS

This research work was funded by Research Institute of University of Riau Grants 2013 for Decentralization funding of Excellent Research Higher Education.

REFERENCE

- Aziz, Azridjal., Kurniawan, Iwan., and Ginting, Hardianto., (2014). Performance of Hybrid Air Conditioning Machine using Condenser Dummy For Water Heater. Annual Seminar in Mechanical Engineering, Indonesian Society of Mechanical Engineering, SNTTM 13th University of Indonesia, paper no. 262. (in Indonesian).
- 2. Hepbasli, Arif., and Kalinci, Yildiz.,(2009). *A review of heat pump water heating system*, Renewable and Sustainable Energy Reviews, Vols. 13, pp. 1211–1229.
- 3. Ji, Jie., Chow, Tin-tai., Pei, Gang., Dong, Jun., and He, Wei. (2003). *Performance of Multi-functional Domestic Heat-pump System*, Applied Thermal Engineering. Vols. 23, pp: 581-592.
- Ji, Jie., Pei, Gang., Chow, Tin-Tai., He, Wei., Zhang, Aifeng., Dong, Jun., and Yi, Hua., (2005). Performance of multi-functional domestic heat-pump system. Applied Energy, Vols. 80, pp: 307-326.
- Kongre, U. V. Chiddarwar, A. Dhumatkar, R. P. C. dan Ari S, A.B., (2013). *Testing and Performance Analysis on Air* Conditioner cum Water Dispenser, International Journal of Engineering Trends and Technology, Vols. 4, pp: 772-775.
- Liu, Fei., Huang, Hui., Ma, Yingjiang., and Zhuang, Rong., (2008). Research on The Air Conditioning Water Heater System, International Refrigeration and Air Conditioning Conference, Purdue University, paper 893.
- Rahman, M. M., Wai Meng, Chin., and Ng, Adrian., (2007).
 Air Conditioning and Water Heating-An Environmental Friendly and Cost Effective Way of Waste Heat Recovery, Journal of Engineering Education, Vols.31, pp: 38-46.
- Sonntag, Richard E., and Borgnakke, Claus., (2009).
 Fundamentals of Thermodynamics. John Wiley & Sonse, Inc.
- Sreejith K., (2013). Experimental Investigation of A Domestic Refrigerator Having Water-Cooled Condenser Using Various Compressor Oils, International Journal of Engineering and Science, Vols. 2, pp: 27-31.
- Stalin, M. Joseph., Krishnan, S. Mathana., and Kumar, G. Vinoth. (2012). Efficient Usage of Waste Heat From Air Conditioner, International Journal of Advances in Engineering & Technology, Vols. 4, pp. 414-423.
- 11. Yi. Xiaowen and W. L. Lee., (2009). The Use of Helical Heat Exchanger for Heat Recovery Domestic Water-Cooled

- Air-Conditioners, Energy Conversion and Management, Vols. 50, pp. 240–246.
- 12. Yilmaz, Mehmet., (2003). Performance Analysis of a Vapor Compression Heat Pump Using Zeotropic Refrigerant Mixtures, Energy Conversion and Management, Vols. 44, pp: 267-282.

Hydroxyapatite Powder Prepared by Low Temperature Hydrothermal Method from Sea Shells

Ahmad Fadli*, Fajril Akbar, Pancasila Putri, Dewi Indah Pratiwi and Ikhbal Muhara

Department of Chemical Engineering, Faculty of Engineering, University of Riau Kampus Binawidya Jl. HR Subrantas Km. 12,5 Pekanbaru 28293 Riau Indonesia

*Corresponding author: fadliunri@yahoo.com

Paper History

Received: 25-October-2014 Accepted: 13-November-2014

ABSTRACT

Hydroxyapatite is bioceramics that widely used in the medical world especially for bone implant and cell culture. Hydroxyapatite was synthesized by low temperature hydrothermal method which sea shells as derived CaO and (NH₄)₂HPO₄ with Ca/P ratio of 0.67, 1.67, 2.67 were heated at 70°C, 80°C, 90°C and stirred at 300 rpm. The obtained paste was dried and then the powder calcined in the temperature range of 700°C - 1000°C. In order to study the morphology and structural characteristics, XRD and SEM were used to estimate the particle size of the powder. FTIR was used to identify organic or inorganic chemicals for estimating the number of components of an unknown mixture. The crystal diameter of hydroxyapatite increased with Ca/P ratio and reaction temperature. Majority hydroxyapatite phase was obtained at Ca/P ratio of 2.67 and 90°C reaction temperature.

KEY WORDS: Hydroxiapatite, hydrothermal, powder, characterization

1.0 INTRODUCTION

Hydroxyapatite (HAP) is the main mineral constituent of teeth and bones [1]. Because of bicompatibility, bioactivity, low solubility in water and ability to replace toxic ions, HAP $(Ca_{10}(PO_4)_6(OH)_2)$ are widely used in biomaterials [2, 3]. Therefore, multiple techniques has been used for preparation of

HAP, including precipitation [4], mechanochemical [5, 6], and hydrothermal [7, 8].

As proposed by Alqap and Sopyan [9], low temperature hydrothermal method provides advantages in comparison other methods due the stable phase of HAP. It poses more convenient method for synthesis HAP with low temperature hydrothermal method than hydrothermal method because it has no need for high temperatures when forming the HAP powder, thus lowering energy costs [10]. It is also more convenient than mechanochemical procedure since low temperature hydrothermal method presents an aqueous phase that is not available in the mechanochemical method. This aqueous phase can accelerate kinetic processes that commonly limit the rate of reaction, such as dissolution, diffusion, adsorption, reaction, and crystallization [11]. The low temperature hydrothermal method also offers variability in particle size by changing the controlled variables such as temperature, pH, rate of stirring, and amount of reactants or Ca/P ratio.

2.0 EXPERIMENTAL

2.1 Materials Preparation

The starting materials in this experiment were ammonium dihydrogen phosphate ((NH₄)H₂PO₄) (Merck, Germany) and sea shell (*Anandara Granosa*) from Pekanbaru local market. Initially, sea shell were cleaned and dried at ambient temperature for 24 hours. Subsequently, dried sea shell was crushed and sieved using a 100-mesh sieve. Sea shells powder were calcinated at 1000°C for 24 hours to changed CaCO₃ to CaO, by these following reaction:

$$CaCO_3 \longrightarrow CaO + CO_2$$
 (1)

2.2 Synthesis of Hydroxyapatite Powder

For the preparation of the solution, CaO and ((NH₄)H₂PO₄ was dropwise in 600 mL distilled water with Ca/P ratio of 0.67, 1.67 and 2.67. The suspension was heated at 70°C, 80°C, 90°C while

stirred at 300 rpm until paste was obtained. Then the paste was dried at 120°C for 15 hours and crushed until powder form. The prepared powders were then calcined in furnace at 900°C. A heating rate of 5°C min⁻¹ was applied until the required temperature was reached and then the heating was continued for 1 hour. Variables in this work were Ca/P ratio (0.67, 1.67 and 2.67) and reaction temperatures (70°C, 80°C and 90°C).

2.3 Characterization

The crystal and phase structures of the samples were identified using a X-ray diffractometer (XRD) with $CuK\alpha$ (λ = 1.5418 Å) incident radiation over the 20 range of 20-60° at room temperature. Moreover, the isolate peaks assigned to (002), (112), and (300) planes were used to estimate the crystallite size (D) of HAP phases, respectively, using the well-known Scherrer's formula as followed [12]:

$$\mathbf{D} = \frac{\mathbf{k}\lambda}{6 \times \mathbf{Cos}\theta} \tag{2}$$

Where k is a shape factor equal to 0.9, λ is the X-ray wave length, β is the full-width at half-maximum (in radians), and θ is the diffraction angle related to the diffraction peak under consideration.

Fourier transform infrared spectroscopy (FTIR) was used for identification of functional groups present in the HAP powder. The morphology and size of the nanoparticles were studied using scanning electron microscopy (SEM)

3.0 RESULTS AND DISCUSSION

3.1 FTIR Spectra

FTIR spectroscopy analysis was also used in this study. FTIR identify the functional groups in the sample. Functional groups that are identified in the FTIR analysis, among others PO₄³⁻, OH, HPO₄²⁻ and CO₃²⁻ in the range 4000 to 600 cm-1 as shown in Figure 1. According Alqap and Sopyan [9] group PO₄ bands appear at wavelengths from 1100 to 1019, 958, 962 and 605 cm⁻¹ in addition to that. In 0.67 Ca/P ratio sample PO₄³⁻ ribbon appears at a wavelength of 953, 1027, and 1067 cm⁻¹. In 1.67 Ca/P ratio sample appears at a wavelength of 962, 1087, 1023 cm⁻¹, whereas in 2.67 Ca/P ratio sample at wavelengths of 963, 1024, and 1086 cm⁻¹ as shown in Figure 1.

In addition PO₄³⁻ group, there are OH⁻ ion appears by FTIR analysis of the samples. Where OH⁻ ion occurs at a wavelength of 3700 - 2500, 630, and 667 cm⁻¹. In 0.67 Ca/P ratio sample OH⁻ group appears at a wavelength of 683 and 612 cm⁻¹. In 1.67 Ca/P ratio sample appears at wavelengths 3572, 3642, 628 cm⁻¹, where as in 2.67 Ca/P ratio sample at a wavelength of 3643 and 630 cm⁻¹. Then there HPO₄²⁻ group contained at wavelengths 1308 and 1260 cm⁻¹ in 0.67 Ca/P ratio sample. Figure 1 also shows clusters at wavelengths 788 and 710 cm⁻¹ which is based on research Alqap and Sopyan [9] at the around that wavelength the functional group that appears was a group of P₂O₇. This proves the presence of calcium pyrophosphate phase.

The results obtained spectrum for each researcher of HAP is different but still in the adjacent values. The results show that there is another group of compounds that should not exist in a

pure hydroxyapatite. Figure 2 shows the FTIR spectrum of synthesized hydroxyapatite with variations in temperature 70°C, 80°C and 90°C. The measurement results of hydroxyapatite synthesized using hydrothermal method with temperature at 70°C using FTIR analysis shown in Figure 2.

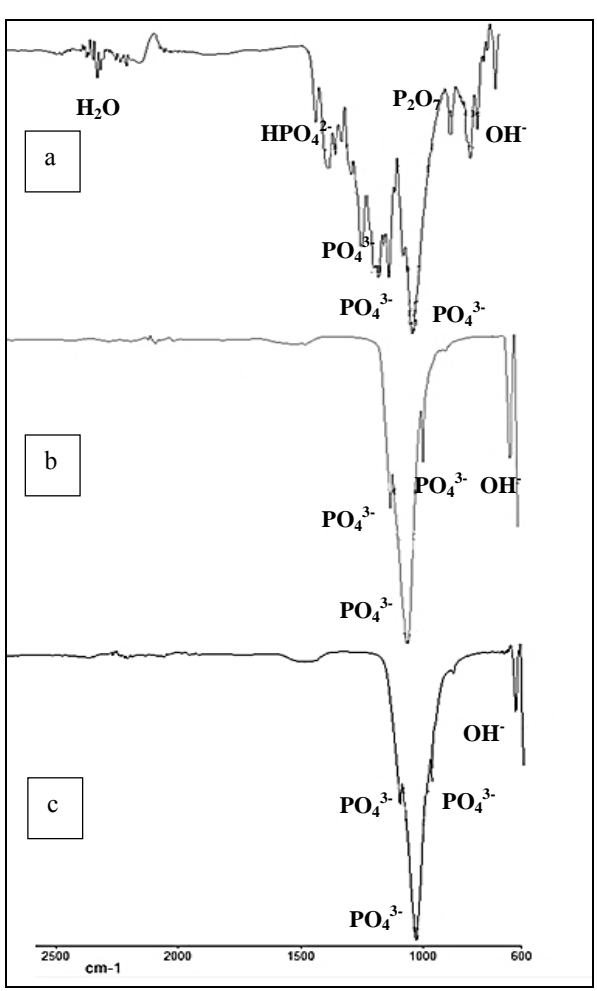


Figure 1 : FTIR spectra of HAP prepared for Ca/P ratio of (a) 0.67 (b) 1.67 and (c) 2.67

Phosphate groups (PO_4^{3-}) asymmetric stretching vibration synthesized detected at wave number $1019~\text{cm}^{-1}$ which indicates that the crystals formed in the synthesis results. In addition, the hydroxyapatite visible spectrum characteristic absorption band around $2021~\text{cm}~H_2O^{-1},\,2167~\text{cm}^{-1}$ and $2182~\text{cm}^{-1}.\,\text{An}$ increase in the intensity of the band $2250\text{-}2000~\text{cm}^{-1}$ which is a band of H_2O on the surface because the surface absorbs water samples HAP. This is possible because the sample storage techniques unfavorable silica gel which does not include the storage time or may also be due to HAP produced from the calcination process becomes more hygroscopic due to the higher calcination temperature. The measurement results of hydroxyapatite synthesized using low temperature hydrothermal method with 2.67~Ca/P ratio using FTIR analysis shown in Figure 2. Phosphate

groups (PO_4^{3-}) asymmetric stretching vibration synthesized detected at wave number $1024~\rm cm^{-1}$ and $1085~\rm cm^{-1}$ which indicates that the crystals formed in the synthesis results. In addition, the hydroxyapatite visible spectrum characteristic of the OH absorption band around 3642 cm⁻¹. This can happen because the HAP powder is hygroscopic, thus precipitating the hydration of the air. OH group at 3642 cm⁻¹ region is called water absorption. Ribbon uptake carbonate (CO_3^{2-}) synthesis were also detected at wave number $1423~\rm cm^{-1}$ which is the asymmetric stretching vibration absorption band is weak with no form of symmetry.

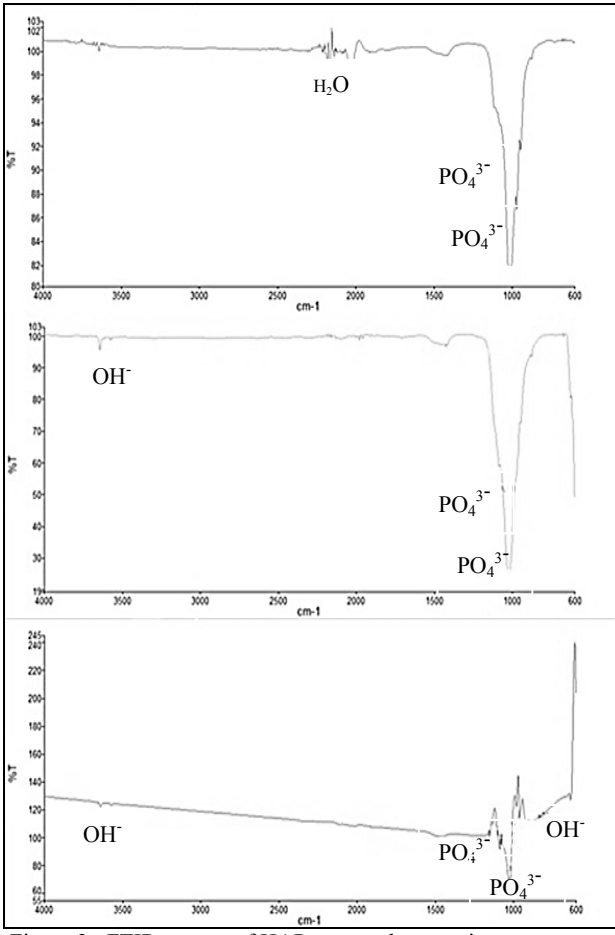


Figure 2 : FTIR spectra of HAP prepared at reaction temperature of (a) 70°C (b) 80°C and (c) 90°C

The measurement results of hydroxyapatite synthesized using hydrothermal method with low temperature of 90°C using FTIR analysis shown in Figure 2. Phosphate groups (PO₄³⁻) asymmetric stretching vibration synthesized detected at wave number 1025 cm⁻¹ and 1241 cm⁻¹ which indicates that the crystals formed in the synthesis results. Ribbon phosphate present in the spectrum of commercial hydroxyapatite as a small band at wave number 878 cm⁻¹, 961 cm⁻¹ and 981 cm⁻¹. In addition, the hydroxyapatite visible spectrum characteristic of the OH

absorption band around 3641 cm⁻¹ and 636 cm⁻¹. This can happen because the HAP powder is hygroscopic, thus precipitating the hydration of the air. OH group at 3641 cm⁻¹ region is called water absorption, whereas the OH groups were detected around the wave number of 636 cm⁻¹ is an illustration of the water absorption. Carbonate absorption band (CO₃²⁻) synthesis were also detected at wave number 1463 cm⁻¹ which is the asymmetric stretching vibration absorption band is weak with no form of symmetry.

3.2 X-ray Analysis

From the results of XRD analysis, it is found that a change in the intensity of the peak from diffractogram. The results of XRD analysis as shown in Figure 3 where for each sample shows the majority present of peaks are hydroxyapatite. Peak of the hydroxyapatite 0.67 Ca/P ratio sample at 20 25.853°, 31.719° and 32.847° with hkl (002), (211) and (300). In the 1.67 Ca/P ratio sample at 20 25.853°, 31.740°, and 32.857° with hkl (002), (211) and (300). And on the 2.67 Ca/P ratio sample at 20 25.879°, 31.739°, and 32.865° with hkl (002), (211) and (300). Where in the peak hkl values are similar to pattern characterization results of XRD analysis from JCPDS (Joint Committee on Powder Diffraction Standards) with PDF Card No. 09-432. In addition, from the data base of results obtained XRD analysis of crystal crystal diameter each sample based on the Scherrer equation, where the crystal diameter grew along with the increasing ratio of Ca/P and temperature is shown in table 1.

Table 1: The average crystallite size of the samples

Ca/P ratio	Reaction temperature (°C)	Crystal diameter (nm)
0.67	90	54.38
1.67	90	52.37
2.67	90	52.32
2.67	70	63.43
2.67	80	55.85
2.67	90	52.48

Based on the analysis of XRD peaks can also be seen other than hydroxyapatite on samples where each sample contains phases as shown in Table 2. In samples with a ratio of 0.67 there is a phase other than the phase composition of hydroxyapatite, the calcium pyrophosphate. The calcium pyrophosphate compound formed by calcium hydroxide derived from the mixing of CaO with water reacts with phosphoric acid, resulting in a calcium dihydrogen phosphate as the following equation:

$$Ca(OH)_2 + 2H_3PO_4 \longrightarrow Ca(H_2PO_4)_2 + 2H_2O$$
 (3)

Then calcium dihydrogen phosphate reacts with ammonia to produce monetite (CaHPO4) or dicalcium phosphate anhydrous (DCPA) as shown in the following reaction:

$$Ca(H_2PO_4)_2 + NH_3 \longrightarrow CaHPO_4 + NH_4H_2PO_4$$
 (4)

Table 2: Phase contained in different Ca/P ratio samples

	-	-			 	 	_	 	 _	 	
	С	a/P	ratio)							

	Mineral phase		
0.67	Hydroxiapatite, Calcium phosphate		
1.67	Hydroxiapatite, Tricalcium phosphate		
2.67	Hydroxiapatite, Calcium hydroxide		

Where monetite (DCPA) is what causes the formation of calcium pyrophosphate. Monetite (DCPA) decomposes into calcium pyrophosphate at a temperature of 700-900°C, this was also a study done by Alqap and Sopyan [9].

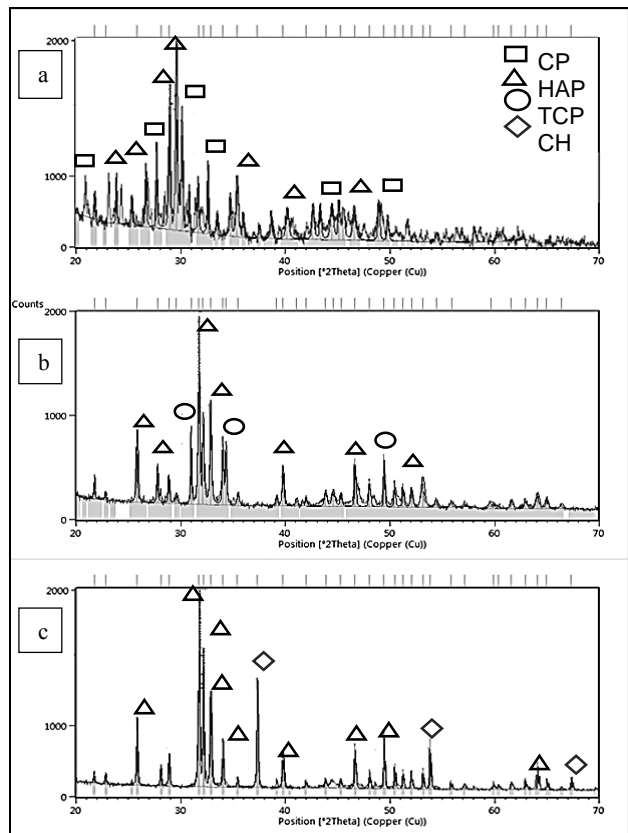


Figure 3 : XRD patterns of HAP at Ca/P ratio of (a) 0,67 (b) 1,67 and (c) 2,67

In samples with a ratio of 1.67 Ca/P phase composition consisting of hydroxyapatite, and tricalcium phosphate. The formation of tricalcium phosphate in 0.67 Ca/P sample is influenced by the ratio of Ca/P in which the ratio of Ca/P is smaller than tricalcium phosphate hydroxyapatite, it is also consistent with studies conducted by Zhang and Darvell [13] where tricalcium phosphate formed in the mass ratio of Ca/P 1.67. Also according Alqap and Sopyan [9] CaO were still present in the sample can cause the formation of tricalcium phosphate and calcium pyrophosphate react like the following reaction:

$$Ca_2P_2O_7 + CaO \longrightarrow Ca_3(PO_4)_2$$
 (5)

While the 2.67 Ca/P sample phase composition was consisting of hydroxyapatite and calcium hydroxide. Where calcium hydroxide CaO derived from mixing with water following reaction:

$$CaO + H_2O \longrightarrow Ca(OH)_2$$
 (6)

3.2 Morphology Sample

From the results of SEM morphology appears apatite crystals that gather several compounds that appear larger with a smooth and uniform grain [14]. Samples with higher heating temperatures produce crystals with a purity higher than samples with lower heating temperatures. Because of the high temperature heating will make the process of better particles growth [15].

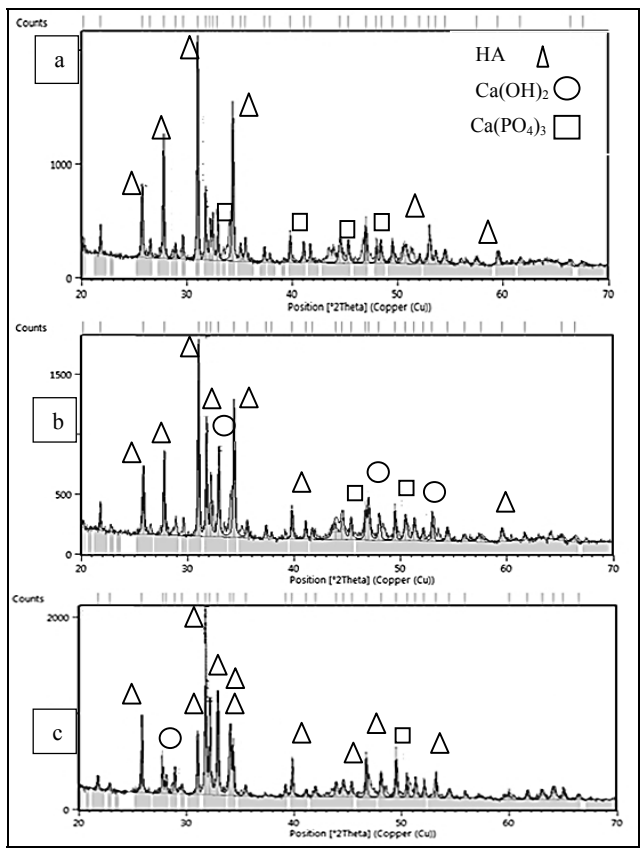


Figure 4 : FTIR spectra of HAP at reaction temperature of (a) 70°C (b) 80°C and (c) 90°C

The sample has a monoclinic and hexagonal crystalline structure. A monoclinic crystalline structure that has an axis that is tilted from its three axes. A axis perpendicular to the axis b; b perpendicular to c, but not c-axis perpendicular to the axis a. All three axes are unequal in length, generally the longest c axis and the shortest axis b. While a hexagonal crystalline structure that has 4 axes of symmetry with the symmetry axis lies in the 3 1

field, which is horizontal. The third axis of symmetry makes an angle of 60° between the horizontal axis and the fourth axis is the vertical axis is cut perpendicular to the axis of symmetry horizontal third. The fourth axis is usually longer than the third horizontal axis. Results of SEM for the results of the synthesis of hydroxyapatite with reaction temperature of 70°C, 80°C and 90°C is shown in Figure 5.

Samples with the SEM observation results using 7500x magnification can be seen in Figure 5. The results of observation samples with reaction temperature of 70°C, 80°C and 90°C (Figure 5) looks like a group of small dense particles. Grain size of the 90°C reaction temperature sample looks smaller than the 70°C and 80°C samples. This is reinforced by the results of the calculation of the size of the crystals from the XRD pattern. Defined as an individual crystal grains. The size of the crystal sample is 63.43 nm where as 70°C reaction temperature sample, 80°C and 90°C samples are 52.85 nm and 52.48 nm. The increase in temperature resulted in an increased thermal vibration energy, which then accelerates the diffusion of atoms through the grain boundaries, small droplets into larger ones. From Figure 5 it can be seen that the distance between the particles are initially very tight show tenuous when the heating temperature is lower.

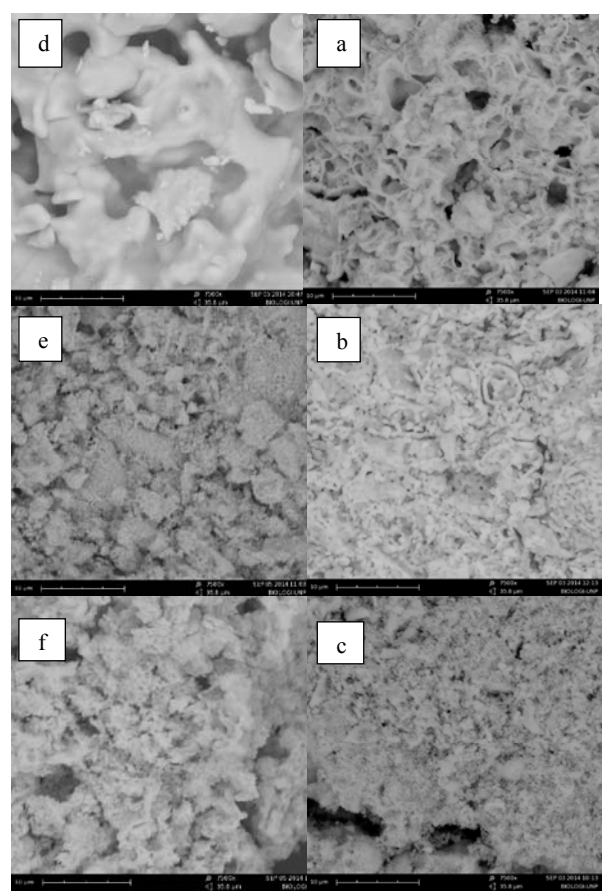


Figure 5: SEM results for sample with reaction temperature of (a) 70°C (b) 80°C, (c) 90°C and Ca/P ratio of (a) 0,67 (e) 1,67 (f) 2.67

Figure 5 shows the results of the samples with variation of the ratio Ca/P.In sample with the Ca/P ratio of 0.67 is shown in Figure 5 d has a larger size than the other samples (1.67 and 2.67 Ca/P ratio samples), this is caused by the presence of some other apatite compounds contained in the sample as has been seen in the results of XRD and FTIR analysis. SEM results also showed that the synthesis of the ratio of Ca/P of 0.67 in both immature hydroxyapatite. SEM result for sample with the ratio Ca/P of 1.67 is shown in Figure 5 e. From the results of SEM photograph looks morphology with finer grains. It is also caused by the presence of other compounds such as tricalcium phosphate apatite were also seen in the results of XRD analysis. For sample with the ratio Ca/P of 2.67 is shown in Figure 5 f. From the results of SEM morphology of the grains appear smoother and more uniform compare to 0.67 and 1.67 Ca/P ratio samples. In accordance with the X-ray diffraction pattern showed that the synthesis of the ratio of 2.67 Ca/P ratio produce hydroxyapatite peaks more than 0.67 and 1.67 Ca/P ratio samples.

4.0 CONCLUSION

Effect of Ca/P ratio and reaction temperature on chemical properties of hydroxyapatite powder from sea shell using low temperature hydrothermal method has been presented the paper. The crystal diameter of HAP at Ca/P ratio of 0.67, 1.67 and 2.67 were 53.38, 52.37 and 52.32 respectively. HAP phase at Ca/P ratio of 2.67 and 90°C temperature reaction was found predominant.

ACKNOWLEDGEMENTS

The authors would like to convey a great appreciation to DIKTI for supporting this research through Hibah Kompetensi 2014..

REFERENCE

- Gosain, A. K., & Persing, J. A. (1999). Biomaterials in The Face: Benefits and Risks. Journal of Craniofacial Surgical 10: 404-14.
- Kuo, T. C., Lee B. S., Kang, S. H., Lin, F. H., & Lin, C. P. (2007). Cytotoxicity of DP-bioglass paste used for treatment of dentin hypersensitivity. Journal of Endodontics 33: 451-454.
- Hench, L. L. (1991). Bioceramics: from concept to clinic. Journal of The American Ceramic Society 74: 1487-510
- Mobasherpur, I., Heshajin, M. S., Kazemzadeh, A., & Zakeri, M. (2007). Synthesis of nanocrystalline hydroxyapatite by using precipitation method. Journal of Alloys and Compounds 430(1-2): 330-333.
- Fahami A., Ebrahimi-Kahrizsangi R., & Nasiri-Tabrizi, B. (2011). Mechanochemical synthesis of hydroxyapatite/titanium nanocomposite. Solid State Sciences 13: 135-141.
- Rhee, S.-H. (2002). Synthesis of hydroxyapatite via mechanochemical treatment. Biomaterials 23(4): 1147-1152.
- 7. Sadat-Shojai, M., Khorasani, M.-T., & Jamshidi, A. (2012). Hydrothermal processing of hydroxyapatite nanoparticles—a taguchi experimental design approach. Journal of Crystal Growth 361: 73-84.
- 8. Zhang, X., & Vecchio, K. S. (2006). Creation of dense

-Science and Engineering-

- hydroxyapatite (synthetic bone) by hydrothermal conversion of seashells. Materials Science and Engineering C 26: 1445-1450
- Alqap A. S. F., & Sopyan, I. (2009). Low temperature hydrothermal synthesis of calcium phosphate ceramics: effect of excess Ca procursor on phase behaviour. Indian Journal of Chemistry 48: 1492-1500.
- Sadat-Shojai, M., Atai, M. & Nodehi, A. (2011). Design of experiments (DOE) for the optimization of hydrothermal synthesis of hydroxyapatite nanoparticles. Journal of Brazillian Chemical 22: 571-582.
- Zhang, X., Vecchio, K. S., Massie J. B., Wang m., & Kim, C. W. (2007). Conversion of bulk seashells to biocompatible hydroxyapatite for bone implants. Acta Biomaterialia 3: 910–918.
- Sopyan, I., Mel, M., Ramesh, S., & Khalid, K. A. (2007).
 Porous hydroxyapatite for artificial bone applications.
 Science and Technology of Advanced Materials 8: 116-123
- 13. Zhang, H., & Darvell, B. W. (2011). Morphology and structural characteristics of hydroxyapatite whiskers: effect of the initial Ca concentration, Ca/P ratio and pH. Acta Biomaterialia 7: 2960-2968.
- Wu, S.-C., Tsou, H.-K., Hsu, H.-C., & Liou, S.-P. (2013). A hydrothermal synthesis of eggshell and fruit waste extract to produce nanosized hydroxyapatite. Ceramics International 39: 8183-8188.
- 15. Moore, W. R., Graves, S. E. & Bain, G. I. 2001. Synthetic bone graft substitutes. ANZ Journal of Surgery 71: 354-361.

Strength Analysis of FPSO's Mooring Lines

C. L. Siow, ^{a,} J. Koto, ^{a,b,*}, H. Yasukawa, ^c A. Matsuda, ^d D. Terada, ^d, C. Guedes Soares, ^e and Muhamad Zameri bin Mat Samad, ^f

Paper History

Received: 12-October-2014 Accepted: 13-November-2014

ABSTRACT

This paper is proposed to discuss the model scale mooring line selection process and preparation for hydrodynamic model experiment. The model scale mooring line should be proper select for model experiment and the error should be minimized because the error in model scale mooring line will be enlarged by the scale factor and influence the design in full scale model. In this study, tensile test experiment for model scale wire ropes was conducted to collect the material properties data of the wire ropes. The data collected from the tensile test is applied to obtain the stiffness of mooring lines in the model scale. To achieve the target to select the model scale mooring lines, the minimum breaking load of the wire ropes and the elongation curve of the wire ropes are collected from tensile test for each wire rope sample. By applying catenary theory and the data from tensile test, the stiffness curve of the mooring line in model scale was estimated. The Difference between the stiffness curve between model scale and full scale is within acceptable at the required experiment range.

KEY WORDS: Tensile Test, Wire Rope, Mooring Line, Catenary Mooring System, Model Experiment.

1.0 INTRODUCTION

In recent development, Liquefied Natural Gas, LNG becomes an

important energy source for human and the demand to the LNG is increasing from year to year. The development of offshore structure suitable for LNG exploration is very challenging and it required complexity analysis and high accurate result in design. To ensure the offloading process which involved multiple floating structures arrangement in small air gap can be safe when the FLNG is operated in open sea, the mooring system for the FLNG must be designed not only able to withstand in rough sea condition also must be able to provide enough restoring force to the FLNG when the shutter tanker come close to the structures.

To ensure the structures design and mooring system design can be worked according to the design condition, model test can be carried out to estimate the safety of whole system before fabricate of the full structure. The model test which completed with the mooring lines and rise in model scale is more preferred if the laboratory facilities are allowed. This is because the involved all the system in the model test can illustrate the response of the structures with more realistic condition when receiving the external load such as wave, wind and current.

In this study, the model scale mooring lines design is focused in this paper. The procedure to selected the model size mooring line and the scaling rule apply is highlighted here. Due to the limited of the reliable data for the suitable wire rope in model size, the tensile test also conducted by this research to collect information to simulate curve of mooring lines. The precaution to conduct the tensile test so the reliable data can be obtained also presented in this paper.

Finally, this paper will also presented the final designed mooring line and the stiffness of the mooring line between model size and full size. The difference between the stiffness of full size and model size stiffness is within the acceptable range and assumed will not cause large difference to the motion response of the model scale experiment which will conduct as the next step in the structures mooring design.

^{a)}Department of Aeronautics, Automotive and Ocean Engineering, Faculty of Mechanical Engineering, Universiti Teknologi Malaysia

b)Ocean and Aerospace Research Institute, Indonesia

^{c)}Department of Transportation and Environmental Systems, Hiroshima University, Japan

d)National Research Institute of Fisheries Engineering (NRIFE), Japan

e)Centre for Marine Technology and Engineering (CENTEC), Instituto Superior Técnico, Universidade de Lisboa, Portugal

Department of Materials, Manufacturing and Industrial Engineering, Faculty of Mechanical Engineering, Universiti Teknologi Malaysia

^{*}Corresponding author: jaswar.koto@gmail.com

2.0 MOORING MODELLING

2.1 Scaling Rule

In this study, the mooring lines in model scale are scaling follow the Froude similarity. Froude's law of similarity is the most appropriate scaling law applicable for the free and moored floating structure experiments. The Froude number has a dimension corresponding to the ratio of u^2/gD where u is the fluid velocity, g is the gravity acceleration and D is a length of the model or prototype. The Froude number Fr is defined as $Fr = u^2/gD$.

Let the subscripts p and m stand for prototype and model respectively and λ is the scale factor, then the scaling for length, speed, mass and force is shown in Table 1.

Table 1: Scaling law between model and prototype

rubie 1. Bearing iaw between model and prototype					
Dimension	Scaling equation				
length, l (m)	$l_p = \lambda l_m$				
speed, u (m/s)	$u_p = \sqrt{\lambda} u_m$				
mass, m (kg)	$m_p = \lambda^3 m_m$				
Force, F (N)	$F_p = 1.025\lambda^3 F_m$				
Mooring line segment weight in water, K (N/m)	$K_p = 1.025\lambda^2 K_m$				

2.2 Modeled Parameter for Mooring Lines

There are three important parameter must be scaled correctly to ensure the mooring lines are properly scaled for the selected environment and the simulation of the structure response is properly scaled to the model size. The parameters of the mooring lines must be scaled as follows [1]

- Pretension of Mooring line
- Stiffness of the mooring designed for the selected site condition
- The restoring force generated by the mooring lines to limit the movement of structures due to external load.

All the three parameter of the mooring system must be scaled to the model scale appropriately to ensure the experiment result is correct represent the structures response.

2.3 Catenary Theory

In the preliminary design, static catenary design method is typically selected to design the catenary type of mooring system for floating structure. To able apply this method to design a mooring system, few assumption of must be applied to the design. The assumptions as follows [2]:

- The seabed condition is fully flat and horizontal
- Bending stiffness of the mooring line can be neglected.
- The mooring lines is only in a vertical plane where involved with X-Z plan only.

The second assumption assumed that the bending stiffness can be neglecting is typically agreed forchain type mooring line. If wire rope mooring line is used in the mooring system, it must be ensure that the curvature curve is small. The catenary model of mooring lines and the axial force acting onevery segment of mooring line is illustrated on Figure 1 and Figure 2respectively.

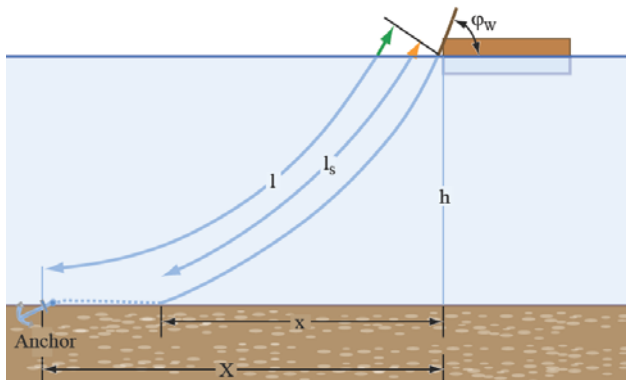


Figure 1: Single Mooring lines [3]

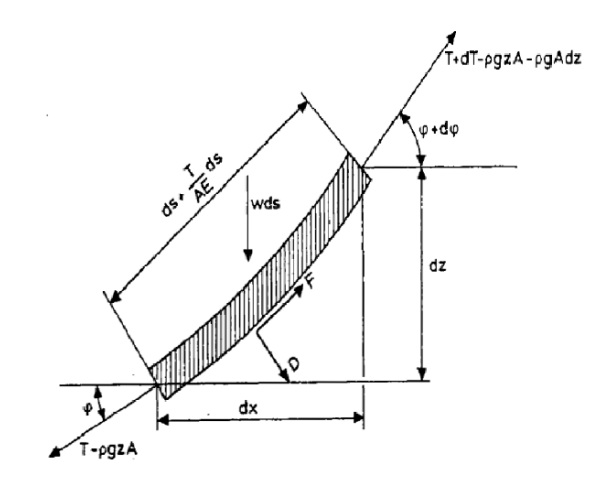


Figure 2: Segment tension of the mooring line

From the Figure 2, w is submerged unit weight/length of mooring line, A is mooring line cross-section area, E is the modulus elasticity of mooring line and T is tension force in line.

The axial tension of mooring line in the segment of mooring line in Figure 2 in static equilibrium condition can be estimated by the following equation [2].

$$dT - \rho gAdz = \left[w \sin \varphi - F\left(1 + \frac{T}{AE}\right)\right] ds \tag{1}$$

$$Td\varphi - \rho gAzd\varphi = w\cos\varphi + D\left(1 + \frac{T}{AE}\right)ds \tag{2}$$

To solve the above equation, the effect from current, D is ignored, hence the equation become

$$T' = T - \rho g z A \tag{3}$$

By solving the equation above, the segment tension of the mooring line become as follow.

$$T = T_H + wh + (w + \rho gA)z \tag{4}$$

In equation (4), h is water depth, T_H is the horizontal tension of mooring line.

The vertical tension of the mooring can be calculated by equation (5)

$$T_z = wl_s \tag{5}$$

If the maximum external load, T_{max} act on the mooring line is known, then the minimum mooring lines length, l_{min} required to ensure the whole mooring line do not fully raise up can be calculated by equation (6)

$$l_{min} = h \left(2 \frac{T_{max}}{wh} - 1\right)^2 \tag{6}$$

Also, the restoring coefficient, C generate by the design mooring line can be calculated from the equation (7) to (9) [3].

$$X = l - l_s + x \tag{7}$$

$$X = l - h \left(1 + 2 \frac{T_H}{wh} \right)^{\frac{1}{2}} + \frac{T_H}{w} \cosh^{-1} \left(1 + \frac{wh}{T_H} \right)$$
 (8)

$$C = \frac{dT_H}{dX} = W \left[\frac{-2}{\left(1 + 2\frac{T_H}{wh}\right)^{1/2} + \cosh^{-1}\left(\left(1 + \frac{wh}{T_H}\right)\right)} \right]^{-1}$$
(9)

2.4 Mooring Line Material Properties Test

From the section 2.3, it is presented the mathematical solution to obtain the mooring line curve and horizontal tension. The required information need to obtain before the mathematical model at section 2.3 are the design parameter such as the length of mooring line, water depth, mooring line material properties.

To obtain the mooring lines material properties, tensile experiment should be conducted to obtain the required information. The information targeted to collect from tensile test are breaking load of wire rope and modulus of elasticity. The example stress-strain curve for wire rope tensile test is shown in Figure 3.

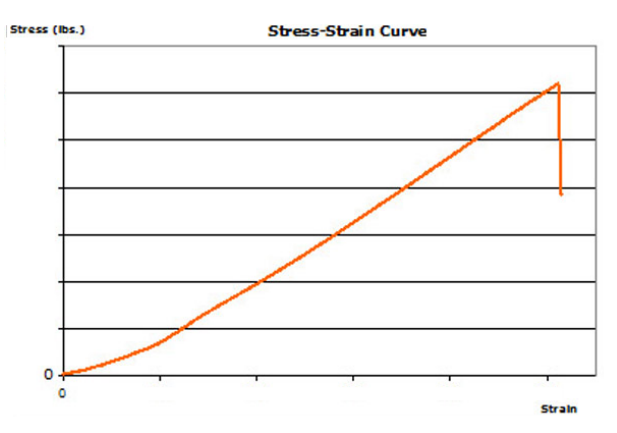


Figure 3: Wire Rope Tensile Test Stress-Strain Curve.

From the Figure 3, the breaking load of the wire rope sample can be obtained from the maximum load apply to the cable. To obtain the modulus of elasticity from the tensile test, Hook law can be applied [4]. According to Hook law, stress is directly proportional to strain.

$$\sigma = E.\varepsilon \tag{10}$$

Where, σ is stress, E is modulus of elasticity and ε is strain. The stress apply in the wire rope can be calculated by equation (11)

$$\sigma = \frac{F}{A} \tag{11}$$

Where, F is the tension force applies to the wire rope, A is the cross section area of wire rope. Also the strain from wire rope can be calculated by equation (12)

$$\varepsilon = \frac{\Delta l}{l_0} \tag{12}$$

Where, Δl the wire rope elongation and l_0 is the initial length of wire rope.

By rearrange equation (10), the modulus of elasticity for the sample wire rope can be calculated as in equation (13)

$$E = -\frac{\sigma}{\varepsilon} \tag{13}$$

3.0 WIRE ROPE TENSILE TEST

Difference to the solid bar tensile test, tensile test for wire rope required more precaution to obtain acceptable result. This is because the wires rope is the roll together by several numbers of strands of metal wire laid. In this situation, the clamping tool for the tensile test and the preparation to the sample need to ensure the load apply to the wire rope can be fully distributed to all strands of metal wire laidand without concentration of force in the single strands of metal wire laidto avoid the wire rope break at the lower tension load condition due to bad distribution of force to all strands of metal wire laid.

To ensure the tension force can be distributed to all the wires in the wire rope, the wire rope end termination is claimed at both the end point of wire rope and then tensile test machine will claim at the wire rope end termination to apply the load to the wire rope during tensile experiment. The end termination applied in this experiment is showed in Figure 4, while the claimed wire rope before the experiment start is showed at Figure 5.



Figure 4: Wire rope with end termination.



Figure 5: Wire rope tensile experiment setup

Besides, there are many factors can be leaded to the failure of tensile test. From the previous experiment, it is facing few failures due to improper experiment setup. The failure face are non-uniform distribute of tension force, breaking in end termination before the wire rope failure and slip. Examples of failure tensile experiment are shown in Figure 6 and Figure 7.



Figure 6: Sample of failure tensile experiment due to breaking of end termination.

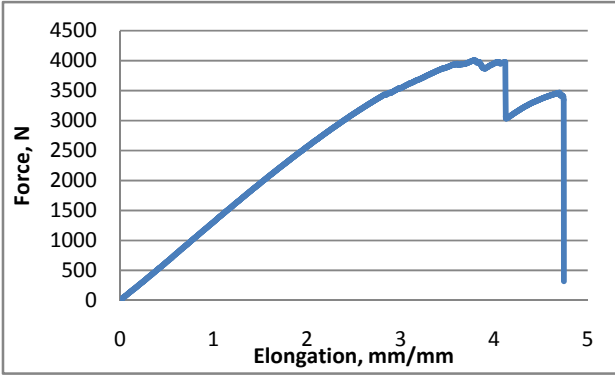


Figure 7: Sample of failure tensile experiment data.

In the tensile experiment, stainless steel wire rope with length of 200mm and nominal diameter of 2mm, 2.5mm, 6mm and 8mm were tested. Sample of success tested wire rope is showed in

Figure 8 and the result from the tensile test for the wire rope nominal diameter 2.5mm and 6mm is showed in Figure 9 and figure 10 respectively.





(2mm Wire rope)

(6 mm wire rope)

Figure 8: Tested wire rope samples.

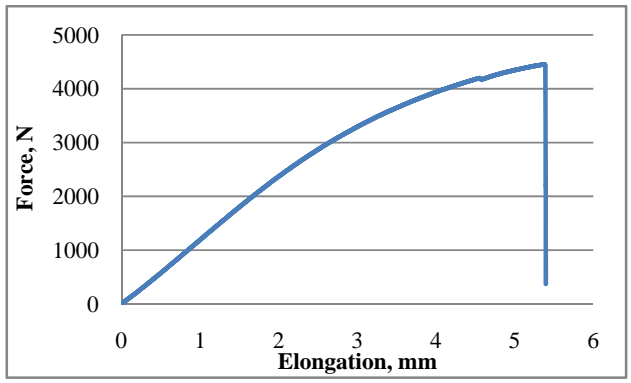


Figure 9: Tensile test result of 2.5 mm nominal diameter wire rope.

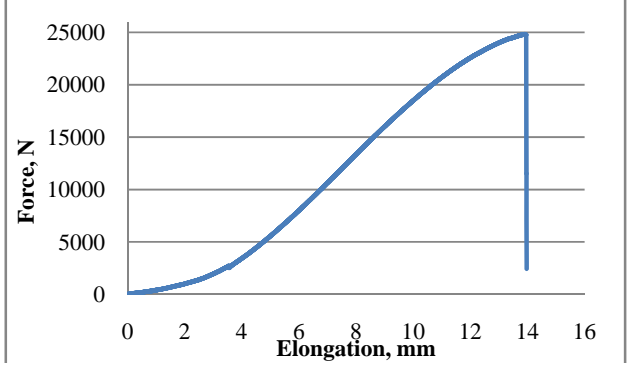


Figure 10: Tensile test result of 6 mm nominal diameter wire rope.

From the tensile test, it is obtained that the modulus of elasticity for the 6-strands wire rope is 61.0 GPa while the standard result for this type of wire rope based on specification is 58.86 GPa [5]. Besides, the minimum breaking load of the wire ropes of nominal diameter 2mm, 2.5mm, 6mm and 8mm are 3.6 KN, 4.5 KN, 24.89KN and 36.25 KN.

4.0 MOORING STIFFNESS

To simulate the effect of mooring to structures motion, the stiffness of mooring lines must be scaled properly. After the elasticity modulus and breaking load of wire ropes in model scale is knew, the calculation on mooring stiffness can be made based on the mathematical model in section 2.3. The final selection of the mooring lines and its properties is showed in Table 2 and Figure 11. And the stiffness is presented in figure 12.



Figure 11: Mooring line profile

Table 2: Mooring line segment information

Particular	Segment A	Segment B	Segment C			
	Model	Model	Model			
Nominal	3.0	3.0	3.0			
Diameter (mm)						
Type	Chain	Wire Rope	Chain			
Segment	4.2	11.3	1.4			
Length (m)						
Air Weight	0.16	0.0369	0.16			
(kg/m)						
Water weight in						
water (kg/m)						
Model scale	0.1425	0.03119	0.1425			
water density:						
1000kg/m ³						
Breaking Load	10.79	5.40	10.79			
(KN)						
Modulus	114.59	61.00	114.59			
Elasticity (GPa)						

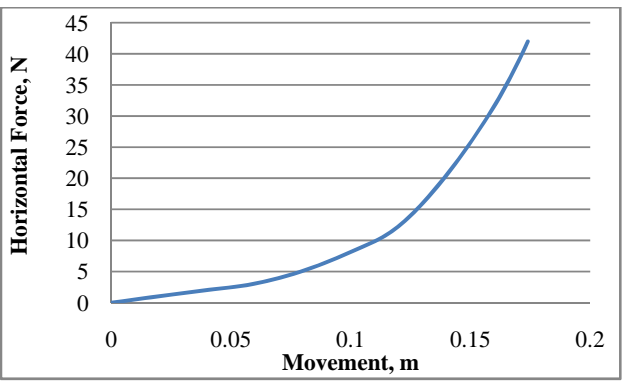


Figure 12: Restoring force from mooring line in model scale.

Besides, the comparison of horizontal restoring force generated by the model scale mooring lines and prototype is showed in Figure 13. The predicted motion of floating structures for the motion experiment is up to 8.5 meters. In the comparison, it can predicted that the motion of floating structures in model scale will slightly larger compared to the actual due to the lower restoring

force provided by the model scale mooring lines.

The slightly difference between both mooring lines is expected because it is impossible to scale the entire particular from full scale to model scale. As example, the scaling of elasticity modulus is difficult to achieve because it involved the material properties of the mooring lines. To ensure the result from the model experiment is reliable, the different of the mooring lines horizontal stiffness is tried to keep as same as possible between models and prototype at the selected test range.

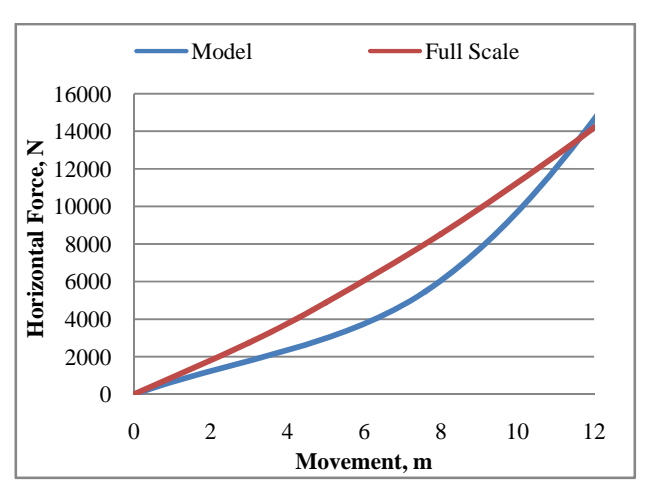


Figure 11: Comparison of horizontal restoring force generated by the model scale mooring lines and prototype.

5.0 CONCLUSION

This paper presented the mooring line preparation to conduct the hydrodynamic tank test. In this study, the static catenary theory is applied to predict the mooring lines stiffness and it generated restoring force to the structure. To able the calculation of mooring lines stiffness be conducted, tensile test of the model scale mooring lines are conducted to obtain the required information such as breaking load of the wire ropes and modulus of elasticity. The precaution of the tensile experiment is taken in this study to ensure the tensile test data is reliable to the calculation. Finally, the comparison of the mooring lines stiffness between model and prototype showed that the model size mooring lines is slightly less stiffness compared to the prototype, however, the difference is still within the acceptable for the range of restoring force required by the tank experiment.

ACKNOWLEGMENT

The authors are very grateful to Tensile Laboratory, Faculty of Mechanical Engineering, Universiti Teknologi Malaysia and Ocean and Aerospace Research Institute, Indonesia for supporting this study.

REFERENCE

1. Subrata Chakrabarti. (1998). Physical Model Testing of

-Science and Engineering-

- Floating Offshore Structures. Dynamic Positioning Conference
- Faltinsen, O.M. (1990). Sea loads on ships and offshore structures: Cambridge, New York: Cambridge University Press. viii.
- 3. MIT open course note (2011), Design of Ocean Systems, Lecture 14: Mooring Dynamics (III).
- 4. R.K. Bansal (1996). *A Text Book of Strength of Materials*: Laxmi Publications.
- 5. Web page:

http://www.certex.co.uk/steelwirerope/steelwireropes/technicalinformation/properties-of-extension-of-steel-wire-ropes (Review in 7 October 2014)

Hydrothermal Synthesis of Hydroxyapatite From Cockle Shell Waste

Yelmida Azis, a,* Zultiniar, Novesar Jamarun, Syukri Arief, and Hadi Nur, a

Paper History

Received: 12-October-2014 Accepted: 13-November-2014

ABSTRACT

The hydroxyapatite synthesis of cockle shell (*Anadara granosa*) as a source of calcium was done by using hydrothermal method. Hydroxyapatite, Ca₁₀(PO₄)₆(OH)₂(HAp) is widely used in medical fields especially as a bone and teeth substitute. First step, the cockle shell were calcined at 900°C for5 hours. The CaO of cockle shell was converted to Precipitated Calcium Carbonated (PCC) by using the carbonation method. The hydrothermal process of PCC was done at 140°C for 16 hours and hydroxyapatite obtained. The forming of biomaterial hydroxyapatite was characterized based on XRD, FTIR, SEM-EDX. The XRD patternsshowed that the products were crystallized hydroxyapatite. The morphology of hydroxyapatite viewed under SEM showed that uniformly crystals of hydroxyapatite.

KEYWORDS: cockle shell, hydroxyapatite, hydrothermal, Precipitated Calcium Carbonated

1.0. INTRODUCTION

Indonesia is very rich with the sources of calcium, both from natural sources (egg shells, corals, cockle shells, bones) and in the form of natural product (limestone) [1]. Kerang darah shells (*Anadara granosa*) is one of the potential calcium sources, a lenient animal (mollusca) of bivalvia class. Moreover, 95% main composition of kerang darah shells is in the form of CaCO₃ [2]. Kerang darah shells' calcium could be processed into the products that are more efficient in the industry or medical world, like

Precipitated Calcium Carbonated (PCC) and hydroxyapatite (HAp).

PCC is a calcium carbonate compound (CaCO₃) that can be processed from the shells material through a series of chemical reactions. PCC particles' is homogeneous that in the same size with micro-scale particle [3]. Currently, PCC widely used in industrial project as an addictive of pharmaceuticals, food, paper, plastic and ink. Previously, PCC has been used as a base material in the synthesis of carbonate apatite. Its high level's purity as well as the small size and constancy of the particles, turn out to be PCC advantage to be changed into apatite compounds [4].

The hydroxyapatite has been broadly used in the biomedical field for filler and coating of bone and dental implants [5,6]. Besides, because of its spongy structure that possess chemical and thermal resistance, the hydroxyapatite has also been widely used as a catalyst or adsorbent [7, 8, 9]. Furthermore, the PCC in this study is made of cockle shells through carbonation method, which will be processed with further method of hydrotermal and synthesized into hydroxyapatite. Based on morphological pattern, particle size and the purity of the Hap powder results, affect the properties of Hap that will be applied in the orthopedics fields, dental materials, as well as for catalyst or adsorbent. It is hoped that through the hydrothermal process, the PCC that made from precursor shellswaste, will be formed HAp that have smooth and identical size, so that it can be usefull in the biomedical field as a bone filler and coating for its tremendous osteoconductivity [5,6].

2.0. MATERIALS AND METHOD

The materials are the cockles shells, which is collected from Indera Giri Hulu, Riau; diammonium hydrogen phosphate ((NH₄)2HPO₄) Merck; 2M nitric acid (HNO₃) solution; ammonium hydroxide (NH₄OH) 65% Merck; CO_2 gas and aquadest. The cockle shell's samples are washed and cleaned, then dried out. After that, it will be mashed up with pulvurizer, and the powder of the cockleshells will be obtained with a smaller seize particle and will be adjusted with a sieve tray (\pm 0.125 mm).

^{a)}Chemical Engineering Department, Riau University, Indonesia¹⁾

b) The Faculty of Mathematics and Science, Andalas University, Indonesia²⁾

^{c)}The Ibnu Sina Institute for Fundamental Science Studies, Universiti Teknologi Malaysia³⁾

^{*}Corresponding author: yelmida azis@yahoo.com



Fig.1 (a) *Kerang darah* shells and (b) powder of *kerang darah* shells

2.1. The formation of PCC by using cockle shells (kerang darah shells)

The cockle shells' powder was calcinated in the furnace around 5 hours at 900°C, and the CaO will be obtained from that process. Then, 16,8 gram of CaO were mixed into erlenmeyer that contains of 300 mL HNO $_3$ 2M solution. After that, the solution will be stimulated with the magnetic stirrer around 30 minutes, before it is finally filtered. In the meantime, filtrate is heated into 60°C, and added thick NH $_4$ OH until it is reaching around pH 12 . The mixture was filtered once again, and to the filtrate the pure CO $_2$ gas was flowed until it is reaching pH 8 and white precipitate or known as PCC was formed. Lastly, the PCC was strained and washed several times by using distilled water. The obtained PCC then dried with ± 115 °C temperature. And it will be ready to be used as the calcium source to synthesize hydroxyapatite [3].

2.2 Synthesis Hydroxyapatite of PCC

The Hydroxyapatite creation of cockle shells' PCC was made according to Hien et al procedure [10], by varying the temperature (120, 140, 160, and 180°C) and time reaction (for 14, 16, 18 and 20 hours) in the *vessel* hydrothermal. Then, 5 gram PCC was added into 15 ml saturated solution (NH₄)₂HPO₄ with mol ratio Ca/P = 1,67. After that, sealed vessel was placed in the oven, and the reaction process will be done in accordance to a suitable variable. The moment reaction is complete, the synthesized solids were cleanly washed by using distilled water, and will be dried out in the oven. On short, the pure dried sample was ready to be characterized.

2.3. Characterization

The characterization of hydroxyapatite will be done through *X-ray diffraction (XRD), Scanning electron microscopy (SEM)(Hitachi S-3400N), Fourier Transform Infrared Spectroscopy (FT-IR).* Not to forget the XRD and SEM analyses of PCC. The analyses of XRD is conducted in order to define the structure of PCC's crystal and the result of HAp synthesis. The SEM image is functioned to look into the morphological surface and the similarity particle of synthesis result of obtained.

3.0. RESULTS AND DISCUSSION

The synthesis of *Precipitated Calcium Carbonated (PCC)* was acquired through modified carbonation method, by adding nitric acid on the calcium oxide dissolution process. Then, the obtained PCC crystals were analyzed by using X-ray diffraction, and the results are compared with the X-ray pattern of cockle shells and standard calcium carbonate, as shown in Figure 2a. 2.b and 2c.

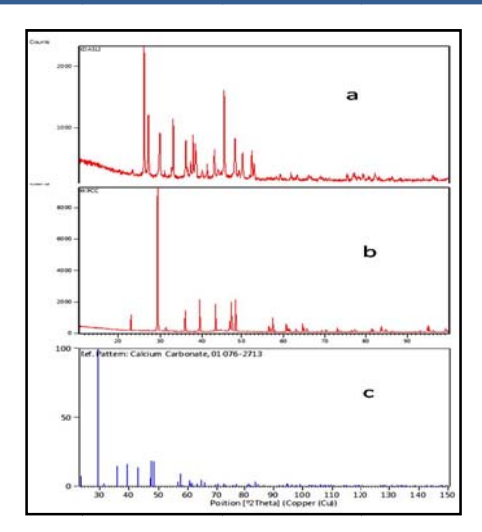


Fig. 2. Diffraction pattern of X-ray: (a) cockle shells,(b).*PCC* of cockle shells,(c).JCPDS calcium carbonate.

Diffraction patterns of X-ray Precipitated calcium carbonated cockle shells will be compared with the JCPDS (01-076-2713) data later. In this process, it is found three peaks with the highest intensity that match the X-ray calcium carbonate standard patterns, around the junction $2\theta = 29.36$; 39.37; 48.46.

SEM image of morphological PCC analyses will be figured below [with enlargement of (a) 100 and (b) 500 times]. The PCC form and size of particles that attained in the research were almost in the same size (20-30 μ meter).

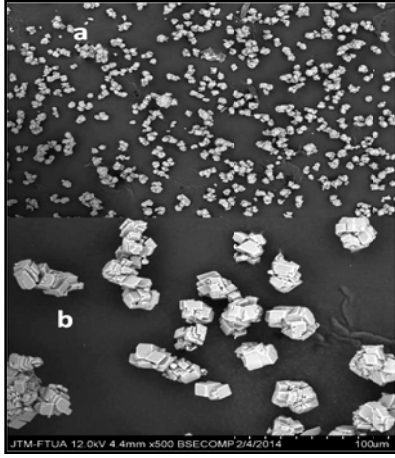


Fig. 3. SEM image of cockle shells' PCC

After that, PCC was utilized as a foundation of hydrothermal process. The temperature were varied (start from 120, 140, 160, and 180°C) and time synthesis (for 14, 16, 18 and 20 hours), as a final point, it was gained the great condition for hydroxyapatite synthesis PCC of cockle shells on 140 °C and 16 hours for the time reaction

Hien et al [10] reported the best condition of coral HAp synthesis stands in the temperature 180°C for 36 hours. This situation could be happen if the coral particles' size were in the large volume (5x5x5 mm) that took a long time and highest

degree of temperature to penetrate ammonium phosphate to form the apatite compound. However, this research used the very fine size of PCC particles, so that the HAp were formed at a midtemperature

The FTIR spectroscopy analyses to the compound of synthesis result on 140° C with time reaction nearby 16 hours, it can be seen the specific spectrum patterns for the PO_4 adsorption of hydroxyapatite (Figure 4.). Meanwhile, in the FTIR spectrum was found the P-O stretching adsorption that came from the $PO_4^{3^{\circ}}$ on 1100-950 cm⁻¹wave number, which known as the characteristics of bands for Hydroxyapatite.In addition, the asymmetric stretching (v) and bending(v4) modes of PO_4^{-3} ion were detected at around 1047.9, and 604.1 and 566.7 cm, respectively.The symmetrical stretching modes (v1 and v2) of PO_4^{-3} ion were also found at around 961.4 and 470.4 cm-1, respectively[5,10].

The analyses spectroscopy result by using FTIR tools shows that there was apatite compound marked with the vibration peak of P-O and PO₄³. The fastening cluster of PO₄³ with the Calcium could be seen with there is no NH band adsorption of ammonia or ammonium on the 3150-3500 cm⁻¹ wave number.

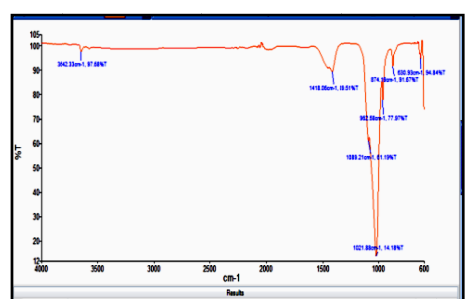


Fig.4. FTIR hydroxyapatite spectrum of cockle shells' PCC

Moreover, an analysis of X-ray diffraction to the compound of synthesis result on the temperature 140° C with time reaction for 16 hours, was directed in order to analyze the obtained apatite compound. The diffractogram apatite compound patterns of synthesis result showed the similar patterns with the XRD standard of hydroxyapatite (JCPDS 01-074-9780) (Figure 5). There, it was revealed some peaks with the high intensity that suitable the X-ray hydroxyapatite standard, which are positioned on 20: 25,87; 28,87; 31,73; 32,86; 33,97; 39,73; 46,66; dan 49,46. Based on that analyses, it can be concluded that the synthesis result of hydroxyapatite own hexagonal crystal system.

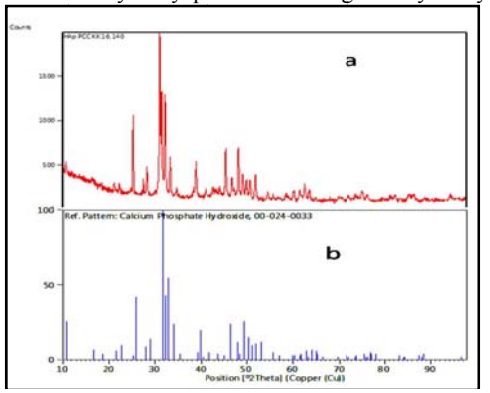


Fig. 5. Diffraction patterns of X-ray(a) hydroxyapatite of synthesis result, (b) standard of JCPDSHydroxyapatite

Figure 6 shows the SEM analysis of apatite compound of cockle shells' PCC on 140°C for 16 hours time reaction [with a. 100, b. 500, c. 1000, and d 1500 times enlargements]

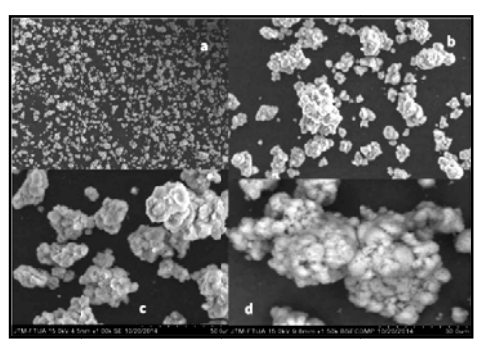


Fig.6. SEM image of hydroxyapatite compound of cockle shells' PCC

The SEM image displayed the synthesis result of hydroxyapatite compound that has the similar form and size of particles (10-50 μ meter).

4.0 CONCLUSION

The compound analysis of synthesis result, proved that the hydroxyapatite synthesis of cockle shells' waste, through the formation of Precipitated Calcium Carbonate (PCC) produced the excellent result. The shortest time of synthesis and the lower temperature degree, illustrates the advantage of the method in this research. Additionally, the tremendous synthesis HAp on140 °C for 16 hours achieved the hydroxyapatite with the Hexagonal crystal structures. As well as the X-ray diffraction patterns and characterization with FTIR are suitable compared with the standard HAp process.

ACKNOWLEDGEMENTS

The authors would like to convey a great appreciation to Dirjen Dikti for supporting this research through Dana Penelitian Desentralisasi 2014

REFERENCE

- Kemperl, J. and Macek, J. 2009. Precipitation of calcium carbonate from hydrated lime of variable reactivity, granulation and optical properties. Int. J. Miner. Process. 93, pp. 84–88
- Rashidi, N.A., Mohamed, M. and Yusup, S.2011. World Academy of Science, Engineering and Technology 60, pp 818-823
- 3. Jamarun, N., Yulfitrin, Arief,S. 2007. Pembuatan Precipitated Kalsium karbonat (PCC) dari Batu Kapur dengan Metoda Kaustik Soda", J.Ris.Kim.,1 (1),20-24
- Ningsih, J.,R.2013. Pemanfaatan Terumbu Karang Dalam Pembuatan Apatit Karbonat dan Karakterisasinya. Thesis Program Pascasarjana Universitas Andalas, Padang
- Ishikawa, K. (2010). Bone Substitute Fabrication Based on Dissolution-Precipitation Reaction. Material.vol. 3: 1138-

-Science and Engineering-

1155

- Bingöl, O.R. and Durucan, C. 2012. Hidrotermal Synthesis of Hidroksiapatit from Calcium Sulfate Hemihydrate, Am. J. Biomed. Sci., vol. 4(1), 50-59
- 7. Garcia, B. Gonzales, G. Ocanto, F. Linares, C. F. 2012. CoMo/Zn-hydroxyapatite as Catalysts for The Hydrodesulfurization reaction of Thiophene. Indian Journal of Chemical Technology, vol.19, pp 403-408
- Vazquez-Hernandez, F., Mendoza-Barrera, C., Altuzar, V. Melendez-Lira, M. Santana-Aranda, M.A., de la, M. and Olvera, L. 2010. Synthesis and characterization of hidroksiapatit nanoparticles and their application in protein adsorption. Material Science and Engineering B, 174, 290-295
- Tsuchida, T., Yoshioka, T. Sakuma, S. Takeguchi, T.,Ueda,W. 2008. Synthesis of Biogasoline from Ethanol over Hydroxyapatite Catalyst.Ind. Eng. Chem. Res.,47, 1443-1452
- Hien, V.D., Huong, D. Q Bich, P. T.N. 2010. Study of The Formation of Porous Hydroxyapatite Ceramics From Corals via Hydrothermal Process. Journal of Chemistry, Vol. 48 (5), P. 591 - 596,



Publishing

ISOMAse Resty Menara Hotel Jalan Sisingamangaraja No.89 Pekanbaru-Riau, INDONESIA http://www.isomase.org/



Editing

Building P-23, Room: 314 Department of Aeronautics, Automotive & Ocean Engineering, Faculty of Mechanical, Universiti Teknologi Malaysia, MALAYSIA http://web1.fkm.utm.my/



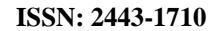
Publication

Teknik Mesin Fakultas Teknik, Universitas Riau, INDONESIA http://www.unri.ac.id/en



Organizing

Ocean & Aerospace Research Institute, Indonesia Pekanbaru-Riau, INDONESIA http://isomase.org/OCARI.php/





Supporting



Mechanical Chapter of the Institution of Engineers, INDONESIA



Malaysian Joint Branch Royal Institution of Naval Architects & Institute of Marine Engineering, Science and Technology -Southern Chapter (MJB RINA &IMarEST – SC)-